Title

Steering the methanol steam reforming performance of Cu/ZrO2 catalysts by modification of the Cu-ZrO2 interface dimensions resulting from Cu loading variation



Authors

Ploner, Kevin

Nezhad, Parastoo Delir Kheyrollahi

Watschinger, Maximilian

et al.

Publication Date

2021-08-01

DOI

10.1016/j.apcata.2021.118279

Peer reviewed

Applied Catalysis A, General 623 (2021) 118279

Contents lists available at ScienceDirect

Applied Catalysis A, General

journal homepage: www.elsevier.com/locate/apcata

# Steering the methanol steam reforming performance of $Cu/ZrO_2$ catalysts by modification of the $Cu\text{-}ZrO_2$ interface dimensions resulting from Cu loading variation

Kevin Ploner [a], Parastoo Delir Kheyrollahi Nezhad [a], Maximilian Watschinger [a], Lukas Schlicker [b], Maged F. Bekheet [b], Aleksander Gurlo [b], Albert Gili [b,c], Andrew Doran [d], Sabine Schwarz [e], Michael Stöger-Pollach [e], Johannes Bernardi [e], Marc Armbrüster [f], Bernhard Klötzer [a], Simon Penner [a,*]

[a] Department of Physical Chemistry, University of Innsbruck, Innrain 52c, Innsbruck, 6020, Austria
[b] Chair of Advanced Ceramic Materials, Institut für Werkstoffwissenschaften und -technologien, Technical University Berlin, Hardenbergstr. 40, Berlin, 10623, Germany
[c] Institute of Chemistry, Technical University Berlin, Sekretariat TC 8, Straße des 17. Juni 124, Berlin, 10623, Germany
[d] Advanced Light Source, Lawrence Berkeley National Laboratory, Berkeley, CA, 94720, USA
[e] University Service Centre for Transmission Electron Microscopy, TU Wien, Wiedner Hauptstr. 8-10, Vienna, 1040, Austria
[f] Institute of Chemistry, Materials for Innovative Energy Concepts, Technical University Chemnitz, Straße der Nationen 62, Chemnitz, 09111, Germany

ARTICLE INFO

*Keywords:*
Monoclinic zirconia
*In situ* X-ray diffraction
$CO_2$ selectivity
Activity
Support

ABSTRACT

On $Cu/ZrO_2$ catalysts, variation of the Cu loading from 0.2 wt% to 80 wt% allows assessing the influence of the $Cu\text{-}ZrO_2$ interface on the methanol steam reforming (MSR) performance by steering Cu particle size and morphology, revealing the contribution of potential active sites at the interface and the intrinsic relative contributions of the support and Cu surface fraction. As $ZrO_2$ influences both $CO_2$-selective and selectivity-spoiling MSR reaction channels, disentangling support-specific effects from the special phase-boundary reactivity and the intrinsic $Cu^0$ reactivity is possible by our approach. By choosing a broad range of Cu loadings, a comparison of the most extreme cases of strong predominance of bulk-like Cu sites (80 wt% Cu) *vs.* highly dispersed Cu (0.2 wt %), dominated by interfacial and support reactivity, becomes accessible. Cu (80 wt%)/$ZrO_2$ evolves as the best MSR catalyst by avoiding adverse support effects and providing a high number of support-wetting bulk-like Cu sites.

## 1. Introduction

Methanol steam reforming (MSR) and methanol synthesis are two of the most promising processes for reversible storage and release of hydrogen [1]. Methanol as chemical hydrogen storage material exhibits a number of advantages over higher alcohols and hydrocarbons. It is liquid at ambient conditions, the absence of a C—C bond allows for a $CO_2$ selectivity close to 100 % and lowers the required reforming temperature (*e.g.* by 100 °C–200 °C *vs.* ethanol) [2], it possesses the highest hydrogen to carbon ratio and both a satisfactory volumetric and gravimetric energy density [3]. The $CO_2$-selective methanol steam reforming reaction (Eq. 1)

$$CH_3OH_{(g)} + H_2O_{(g)} \rightleftarrows 3\,H_{2,(g)} + CO_{2,(g)}\ \Delta H_r^0 = 49.6\text{kJ mol}^{-1} \quad (1)$$

is impaired by potential parasitic $CO_2$-lowering side reactions such as the reverse water-gas shift reaction, methanol dehydrogenation to CO and the subsequent partial methanation of intermediately formed CO and $CO_2$ [4,5]. Direct steering toward high $CO_2$ selectivity is crucial to obtain a high hydrogen yield and avoiding the potential catalyst poison CO [2,6].

The commercially available $Cu/ZnO/Al_2O_3$ methanol synthesis catalyst exhibits a high $CO_2$ selectivity (*e.g.* > 99 % at 90 % methanol conversion and 306 °C [7]) in MSR, but produces too high levels of CO for direct use of the reformate in *e.g.* polymer electrolyte membrane fuel cells [8]. As MSR runs at higher temperatures than the synthesis reaction, it suffers from rapid on-stream deactivation due to Cu particle sintering [2]. $Cu/ZrO_2$, on the other hand, has evolved as an alternative

* Corresponding author.
*E-mail address:* simon.penner@uibk.ac.at (S. Penner).

https://doi.org/10.1016/j.apcata.2021.118279
Received 13 May 2021; Received in revised form 24 June 2021; Accepted 27 June 2021
Available online 1 July 2021

catalyst material exhibiting excellent MSR performance [9,10].

The combined micro- and electronic structure control of metallic Cu *via* the specific Cu/support interface and the oxygen content are discussed as the most important activity and $CO_2$ selectivity steering parameters [2,11]. The exact operational role of ionic *vs.* metallic Cu species is still subject to controversial discussion. Structurally ordered and chemically pure metallic copper is inactive in MSR [12]. Hence, the active form of copper is related to a non-equilibrium state of metallic Cu [11]. The presence of ionic Cu species and purely geometrical strain effects are offered as explanations for high activity and $CO_2$ selectivity and are related to synergistic Cu interactions with the support resulting mainly from catalyst preparation [11].

Beyond the exact structural and redox state of Cu, the Cu particle size and loading significantly affect the catalytic performance. Attempts to model and unravel the role of the Cu/$ZrO_2$ interface by varying the copper loading suffer from the poor definition of the initial crystal structure and disparate preparation of $ZrO_2$ [13–15]. Amorphous $ZrO_2$ or mixtures of the monoclinic and the tetragonal $ZrO_2$ (t-$ZrO_2$) are all employed. The variation and at the same time narrow compositional range of the Cu loading utilizing the same synthesis routine and sample treatments essentially yield different optimized Cu contents. A loading of 80 wt% CuO on a structurally heterogeneous $ZrO_2$ support yielded superior MSR performance in terms of hydrogen production [13]. On the contrary, Takezawa et al. obtained the highest $H_2$ turnover frequency for a loading of 7.78 wt% Cu on a similarly heterogeneous $ZrO_2$ support [14]. A methanol conversion increase with increasing Cu content up to 16 wt% Cu for Cu/t-$ZrO_2$ catalysts containing traces of m-$ZrO_2$ was also reported [15]. Only Ritzkopf et al. explicitly account for the $CO_2$ selectivity, observing an increased CO content in the product stream with increasing Cu loading at a temperature of 300 °C [15].

The chemical state of Cu during both the reforming and partial oxidation of methanol (POM) has been discussed as a crucial parameter, where especially ionic $Cu^+$ species have been reported to be particularly selective. Agrell et al. conducted partial oxidation of methanol on a Cu/ZnO/$ZrO_2$/$Al_2O_3$ catalyst and observed the formation of $Cu^+$ by *pseudo in situ* XPS measurements upon exposure to the reaction mixture (1:2). Oxidized Cu, coexisting with metallic copper [7], is claimed to represent the active Cu species under POM conditions. This interpretation is challenged by NAP-XPS studies revealing subsurface oxygen as the crucial Cu-activating species, which can only be observed *in situ*, rather than inactive Cu oxides [16]. Investigations on a commercial Cu/ZnO/$Al_2O_3$ catalyst under different reaction conditions yielded a dependence of the post-reaction oxidation state of copper on the feed gas composition and the temperature. Substantial hydrogen production upon the presence of either $Cu^\circ$ or $Cu^+$ was displayed [17]. On Cu/$ZrO_2$, the formation of elemental Cu after prolonged MSR operation at 250 °C is reported to depend on both Cu loading and methanol:water ratio [13,18]. The best $H_2$ yield was obtained using 80 wt% CuO on again structurally poorly defined $ZrO_2$. This $ZrO_2$-supported catalyst almost exclusively revealed the presence of $Cu_2O$, which was suggested to exhibit superior MSR properties [13,18]. We note that that the conclusions were essentially inferred from *ex situ* characterization, which naturally raises concerns about the stability of *e.g.* potential metallic active sites upon exposure to air.

Therefore, in general, *in situ* and *operando* methods must be utilized to clarify the role of the active centers. In this manuscript, the recurrent methodological theme using *in situ* X-ray diffraction (XRD) in combination with *ex situ* X-ray photoelectron spectroscopy (XPS) and electron microscopy (TEM and SEM) is employed.

As $ZrO_2$ can act as a particularly suitable support for Cu to steer methanol steam reforming toward optimum $CO_2$ selectivity, we set out to scrutinize the influence of the Cu-$ZrO_2$ interface- and relative surface dimensions on the MSR performance. To provide the most defined catalyst starting state possible, well-ordered monoclinic zirconia (m-$ZrO_2$) was selected as the most promising support based on previous studies with respect to high $CO_2$ selectivity [19]. The Cu morphology (as a direct consequence of Cu loading) and its direct correlation to the Cu bulk and surface oxidation state in combination with the influence of the support chemistry to optimize the $CO_2$ selectivity is the central goal of the presented work. The variation of the Cu metal loading allows controlling both Cu particle size and Cu morphology. The contribution of potential active sites at the Cu-$ZrO_2$ interface, as well as of the intrinsic relative contributions of the support and Cu surface fraction, are equally accessible. Based on recent studies [19], it is clear that $ZrO_2$ is an active support, influencing both the $CO_2$-selective and selectivity-spoiling reaction channels of the overall reaction mechanism. By using the same monoclinic $ZrO_2$ support it was possible to discriminate support-specific effects from the special phase-boundary and the intrinsic reactivity of metallic Cu. Choosing the full range of Cu loadings makes a comparison of the most extreme cases possible: on the one hand, the strong predominance of the intrinsic Cu surface area contributions (that is, almost all Cu sites are located within a bulk-like Cu environment and interfacial and support surface site contributions are accordingly minimized) can be assessed. On the other hand, the opposite scenario of almost atomic-scale dispersion of Cu is accessible. Hence, the full compositional range from 0.2 wt% to 80 wt% Cu is focused upon in the presented study to provide a more comprehensive investigation of the influence of the Cu loading in MSR. By using a phase-pure, structurally and chemically invariant support, this strategy allows for unambiguous discrimination of selectivity-promoting/spoiling contributions of the support inter- and surface *vs.* the intrinsic $Cu^\circ$ contribution (which becomes predominant at high loadings).

## 2. Experimental

### 2.1. Catalyst synthesis

All catalysts were prepared following a similar procedure based on standard aqueous impregnation. An aqueous solution (6 g $l^{-1}$ for all except 0.2 wt% with 0.6 g $l^{-1}$) of Cu(II) acetate (Merck) is slowly added to a stirred aqueous suspension (volume ratio solid/liquid of approximately 1:100) of monoclinic (m-)$ZrO_2$ (Alfa Aesar, 99.978 %). Subsequent removal of the solvent at 60 °C, drying *in vacuo* and calcination in air at 400 °C for 2 h results in the formation of the CuO/$ZrO_2$ precatalysts. Different ratios corresponding to 0.2 wt% to 80 wt% $Cu^\circ$ after pre-reduction were used to prepare the individual catalysts. For an overview of the Cu loading of all samples, we refer to Table 1 in Section 3.

### 2.2. Catalytic testing

All catalytic tests were performed in a dedicated all-quartz recirculating batch reactor. The gas phase composition is monitored *via* a capillary leak to a quadrupole mass spectrometer (QMS, Balzers QMG 311) arranged in cross-beam geometry and equipped with a secondary electron multiplier. The small reactor volume (13.8 mL) allows the detection of trace by-products and the characterization of small sample amounts (10 mg – 100 mg). Heating is performed using a Linn High

**Table 1**
Overview of the studied samples with the nominal copper loading and the values according to ICP-OES in the calcined state.

| Sample name | Nominal copper loading (reduced state, $Cu^0$) / wt% | Nominal copper loading (calcined state, CuO)/ wt% | Copper loading from ICP-OES (calcined state) / wt% |
|---|---|---|---|
| CmZ02 | 0.2 | 0.2 | 0.2 |
| CmZ2 | 2.0 | 2.0 | 2.0 |
| CmZ20 | 20 | 19 | 19 |
| CmZ40 | 40 | 36 | 36 |
| CmZ80 | 80 | 67 | 71 |

C = Cu; mZ = m-$ZrO_2$, the number refers to the nominal copper loading after pre-reduction.

Term furnace capable of operating up to 1100 °C, where the temperature is monitored *via* a K-type thermocouple (NiCr-Ni) near the sample.

To prevent condensation, the MSR reaction mixture is introduced at 100 °C by expansion of the gas phase over a 1:10 liquid methanol/water mixture (resulting in a methanol:water ratio of 1:2 in the gas phase at room temperature). The liquid mixture is degassed by several freeze-and-thaw cycles. Standardized oxidative cleaning procedures in 1 bar pure oxygen at 400 °C for 1 h (termed "O400") and a pre-reduction treatment in 1 bar pure hydrogen at 300 °C for 1 h (termed "H300") are performed before the MSR reaction mixture (≈ 28 mbar) is introduced. Ar (≈ 6 mbar) for time-dependent QMS intensity correction (to compensate the steady gas withdrawal through the leak into the mass spectrometer) and He as carrier gas to improve the recirculation efficiency and the heat transfer are subsequently added. During MSR, the gas phase composition is continuously quantified by mass spectrometry. The Ar $m/z = 40$ corrected intensity *vs.* time data, in combination with external calibration of the relevant gases, including their relative fragmentation patterns, yield the partial pressure changes *vs.* time of the reactants and products. Normalization of the reaction rates to the Cu surface sites has been performed to calculate turnover frequency numbers. We outlined the calculation of the turnover frequency (TOF) values in Section A in the Supporting Information.

### 2.3. Powder X-ray diffraction (PXRD)

*Ex situ* powder X-ray diffraction measurements were carried out on a Stadi P diffractometer (STOE & Cie GmbH, Darmstadt, Germany) in transmission geometry. A MYTHEN2 DCS6 detector system (DECTRIS Ltd., Switzerland) and a Mo X-ray tube (GE Sensing & Inspection Technologies GmbH, Ahrensburg, Germany) with 40 mA and 50 kV were used. Mo-$K_{\alpha 1}$ radiation with a wavelength of 0.7093 Å was selected using a curved Ge(111) crystal. Evaluation of the data was performed using the WinX$^{POW}$ software [20]. Phase analysis was based on references from the ICDD database [21]. Synchrotron-based *in situ* XRD investigations for the characterization of the copper bulk phase evolution in MSR were conducted at the beamline 12.2.2 at the Advanced Light Source (ALS) at the Lawrence Berkeley National Laboratory (LBNL), California. The measurements were performed with a Perkin Elmer image plate detector collecting one pattern per 180 s in transmission mode with a monochromatic 25 keV beam of 30 µm spot size. A $LaB_6$ NIST standard was used for calibration of the sample-to-detector distance, the detector tilt and the exact wavelength (0.4982 Å) in the Dioptas software [22]. Additionally, the two-dimensional detector images were integrated to obtain powder diffraction patterns with the same software.

The samples were placed in capillaries (inner diameter =700 µm) and heated with two infrared lamps illuminating a SiC sleeve [23]. The gases for pre-oxidation (pure $O_2$, 10 mL min$^{-1}$, 400 °C, 60 min) and pre-reduction (pure $H_2$, 10 mL min$^{-1}$, 300 °C, 60 min) were supplied with the setup described by Schlicker et al. in [24]. For the *in situ* MSR measurements, a liquid mixture of methanol:water = 1:10 was heated to its boiling point in an Erlenmeyer flask. This provides a gas phase composition of methanol:water = 1:2, which is seeded in He carrier gas (5 mL min$^{-1}$) and passed to the sample through a heated tube to prevent condensation. In this atmosphere, the temperature was increased from 120 °C to 350 °C with a rate of 10 °C min$^{-1}$, followed by an isothermal period of 20 min. Pure He (15 mL min$^{-1}$) for cooling was provided through a different line to avoid further introduction of the MSR mixture into the capillary. The Rietveld refinement (RR) of the XRD data was conducted utilizing the FullProf software [25]. The profile function 7 (Thompson-Cox-Hastings pseudo-Voigt convoluted with an axial divergence asymmetry function) [26] was used in all refinements. The resolution function of the diffractometers was obtained from the structure refinement of the $LaB_6$ NIST 660b standard.

### 2.4. Determination of the specific surface area

Measurements of the specific surface area based on the BET method were performed with a NOVA 2000e Surface Area & Pore Size Analyzer (Quantachrome Instruments) using the software Quantachrome NovaWin. The samples were heated to 200 °C *in vacuo* for 30 min before the adsorption of $N_2$ at −196 °C at five points from 0.05 $p/p_0$ to 0.3 $p/p_0$ was conducted.

### 2.5. In situ thermogravimetric analysis (in situ TGA)

The *in situ* TG measurements were performed with a NETZSCH STA 449F3 Jupiter TGA/DSC setup equipped with Ar, $O_2$ and $H_2$ (all gases 99.999 % from Linde). The differential TG (DTG) curves were obtained by differentiating the mass change with respect to the temperature. The samples were pre-oxidized in 5% $O_2$ in Ar (total flow 100 mL min$^{-1}$) by heating to 600 °C with 5 °C min$^{-1}$, followed by an isothermal period of 30 min to ensure quantitative oxidation to CuO. The reduction behavior was investigated by treating the samples in 10 % $H_2$ in Ar (total flow 100 mL min$^{-1}$) starting at 25 °C at a heating ramp of 5 °C min$^{-1}$ up to a final temperature of 300 °C. An isothermal period ensures full reduction and enables deducing the Cu loading from the mass loss. An additional oxidation step after reduction up to 600 °C in 5% $O_2$ in Ar (total flow 100 mL min$^{-1}$) with a ramp of 5 °C min$^{-1}$ indicates intermediary $Cu_2O$ formation before full oxidation to CuO. The mass increase in this measurement is utilized to corroborate the value of the copper loading by ICP-OES.

### 2.6. Inductively coupled plasma optical emission spectroscopy (ICP-OES)

The Cu loading of the catalyst was determined by ICP-OES employing a Varian Vista RL instrument. As the solvent of the copper phase, freshly prepared aqua regia (hydrochloric acid, 37 %, nitric acid, 68 %, VWR chemicals AnalaR NORMAPUR) was utilized and diluted with water to a concentration of 5% prior to analysis. The calibration was performed for a concentration range from 20 mg l$^{-1}$ to 100 mg l$^{-1}$ by dilution of a copper standard solution.

### 2.7. Determination of the specific Cu surface area via dissociative $N_2O$ adsorption

The dissociative adsorption of $N_2O$ on metallic Cu is used for the quantitative determination of the accessible surface area by selective oxidation of the topmost layer to $Cu_2O$ [27–29]. The $H_2$ consumption during the reduction following this procedure is utilized for quantification. The samples are loaded into an all-quartz reactor and its effective volume is calibrated with the expansion of He (5.0, Messer) at the reduction temperature of 300 °C. An initially degassed zeolite trap in the cold zone of the reactor removes the reaction-formed water. Initially, all samples are pre-reduced in flowing $H_2$ (5.0, Messer) for 30 min at 300 °C, which yields metallic Cu on all catalysts. After evacuation, the reactor is purged with He and re-evacuated. Following cooling down *in vacuo* to 70 °C, a defined pressure of $N_2O$ (2.0, Messer) monitored by a Baratron pressure transducer (MKS Instruments) is provided in a manifold. The consumption of $N_2O$, as well as the evolution of $N_2$, is monitored by a quadrupole mass spectrometer (QMS) from Balzers (QMA125; QME 125-9) for 30 min after opening the valve to the sample. The temperature is subsequently increased to 300 °C after evacuation and flushing with He. A defined amount of $H_2$ is introduced into the reactor and the pressure decrease resulting from reduction of the newly formed surface $Cu_2O$ is observed for 35 min. The calculation of the specific Cu surface area from $N_2O$ adsorption is discussed in detail in Section A in the Supporting Information.

### 2.8. Transmission and scanning electron microscopy (TEM and SEM)

Structural and chemical transmission electron microscopic (TEM) analysis was performed using a FEI TECNAI F20 field emission TEM operated at 200 kV, equipped with a high angle annular dark-field STEM detector (HAADF), an Apollo XLTW SDD X-ray detector and a GATAN GIF Tridiem image filter. The spatial resolution of the EDX maps is about 1 nm. For SEM experiments, a FEI Quanta 250 field emission SEM was used. Prior to SEM imaging, the samples were coated with 10 nm Au/Pd to improve their conductance.

### 2.9. X-ray photoelectron spectroscopy (XPS)

A Thermo Scientific MultiLab 2000 spectrometer with an Alpha 110 hemispherical sector analyzer and a monochromatic Al $K_\alpha$ X-ray gun is employed for the XPS investigations. A flood gun supplies electrons with a kinetic energy of 6 eV for charge compensation and the base pressure is kept in the low $10^{-9}$ mbar range. Detailed scans of the most relevant regions were recorded with a pass energy of 20 eV and an energy step size of 0.05 eV. For background correction, a Shirley-type function is utilized. The quantitative determination of the surface composition is based on high-resolution Zr 3d and Cu $2p_{3/2}$ spectra using the relative sensitivity factors (RSFs) [30] as well as the different inelastic mean free paths using the predictive G1 formula according to Gries [31]. Reference samples of various Cu species were measured using the same instrument for qualitative assignment of the Cu state, including metallic Cu (sputter-cleaned Cu foil, Goodfellow, $\geq$ 99.99 %), $Cu_2O$ (Sigma-Aldrich, anhydrous, $\geq$ 99.99 % trace metals basis), CuO (Sigma-Aldrich, 99.999 % trace metals basis) and $Cu(OH)_2$ (synthesized by precipitation with $CuSO_4 \bullet 5\ H_2O$ (Merck, for analysis, 99.7 %) and NaOH (Roth, $\geq$ 99 %)).

## 3. Results and discussion

To ensure optimized comparability, in addition to the identical synthesis route, exactly the same pre-treatments and MSR conditions were applied to all systems. A complete sample list is provided in Table 1. The deviation of the loading of CmZ80 determined by ICP-OES in the calcined state is a consequence of its phase composition, which is not exclusively CuO (as demonstrated by XRD, see SI Table S1). The lack of oxygen will therefore result in an apparently higher Cu content in this catalyst. The same is observed for CmZ40 and CmZ20 (see Table S1). The higher the amount of $Cu_2O$, the larger the deviation from the nominal copper loading. As the deviation is not observed in the reduced state, the correlation to incomplete Cu oxidation is evident.

### 3.1. (Copper) surface area, dispersion and average particle size

The results of the characterization of the total and Cu surface area, including its dispersion and its average particle size, are listed in Table 2. As Cu in its metallic state is required for this method, the catalysts were pre-reduced in $H_2$ at 300 °C prior to contact with $N_2O$ (see Section 2.7), where no intermediate exposure to air occurred at any stage of the experiment. The BET surface area of all catalysts, which was determined in the calcined state, is in the same range. A similar trend is found for the specific copper surface area: only a factor of 2 separates CmZ02 and CmZ80, whereas the Cu loading of these catalysts varies by a factor of 400. These observations translate to drastically different values for the copper dispersion and average particle size. While Cu is highly dispersed and exhibits particles with only a few nanometers in diameter in CmZ02, the former decreases and the latter increases continuously with increasing Cu loading. CmZ80 displays a very low dispersion of copper and the assumption of embedded hemispherical particles used for the estimation of the average particle size is not valid anymore (see TEM/SEM characterization in Fig. 1). Due to the extreme variation of the dispersion, the estimation of TOF values is essential for the comparison of the catalytic performance of the five samples. We specifically note that none of the $N_2$ adsorption isotherms indicated the presence of highly porous materials.

**Table 2**
BET surface area, specific copper surface area, copper dispersion ($D_{Cu}$) and average copper particle size ($d_{Cu}$) of the investigated $Cu/ZrO_2$ catalysts.

| Sample | BET surface area [*1] / $m^2$ $g_{Cat}^{-1}$ | $SA_{Cu}$ [*2] / $m^2$ $g_{Cat}^{-1}$ | $D_{Cu}$ [*2] / % | $d_{Cu}$ [*2] / nm |
|---|---|---|---|---|
| CmZ02 | 3 | 0.18 | 18 | 3 |
| CmZ2 | 4 | 0.23 | 1.8 | 30 |
| CmZ20 | 4 | 0.24 | 0.19 | 270 |
| CmZ40 | 2 | 0.35 | 0.15 | 350 |
| CmZ80 | 1 | 0.41 | 0.09 | 580 |

[*1] determined after calcination of the catalysts.
[*2] presence of metallic Cu is required, so the catalysts were pre-reduced in $H_2$ at 300 °C; BET surface area of pure m-$ZrO_2$: 1 $m^2$ $g^{-1}$.

In summary, while the specific surface area of copper increases slightly with higher Cu loading, the copper dispersion displays a continuous decrease from 0.2 wt% to 80 wt% Cu. This trend translates to different initial Cu states of the samples for MSR in terms of the average copper particle size.

### 3.2. Structural characterization of the calcined $Cu/ZrO_2$ catalysts by electron microscopy and X-ray diffraction

The SEM and TEM characterization of the Cu/m-$ZrO_2$ catalysts with different Cu loadings ranging from 0.2 wt% to 80 wt% in their calcined state is highlighted in Fig. 1. To show the variation of the Cu distribution as a function of loading, we rely on EDX mapping of representative catalyst regions at different representative scales. As expected, the Cu distribution and morphology transform from essentially uniform and highly dispersed (uppermost panel, CmZ02) over Cu nanoparticles (second panel from the top, CmZ2) to Cu wetting and covering large areas of the individual m-$ZrO_2$ grains (third, fourth and bottommost panel, CmZ20, CmZ40 and CmZ80). For higher Cu loadings, Cu also acts as a "glue" between the grains of the m-$ZrO_2$ support.

Some isolated Cu particles are also observed for the lowest Cu loadings (Fig. 2, upper panel). The lower panel of Fig. 2 features an exemplary evaluation of the Cu bulk oxidation state for the CmZ80 *via* EELS mapping experiments. Correlation of the featured total Cu-L intensity (using electrons with a characteristic energy loss) with the intensity of those Cu electrons with a defined energy loss characteristic for CuO and $Cu_2O$ reveals at least partial oxidation of the $ZrO_2$-wetting and -encapsulating metallic Cu islands. The TEM data are in full accordance with the XRD data and the obtained dispersion.

The microscopy results corroborate the trends observed in the copper dispersion, where a transition from highly dispersed Cu at 0.2 wt% over nanoparticles (CmZ2) and formation of copper islands (CmZ20 and CmZ40) to encapsulation and considerable wetting of the zirconia support by Cu is observed. This variation in the copper morphology with the loading provides a means to tune the catalyst properties regarding the Cu particle size as well as the fraction of exposed support, which is reflected in the different behavior in MSR (see Section 3.3). Additionally, changes to the Cu morphology after MSR were recorded by TEM (Fig. S1, see SI), in direct accordance with Fig. 1. No alterations in all the samples, except for CmZ02, were recognized, directly confirming their structural and morphological stability. The TEM image of Fig. 2 reveals the presence of some isolated Cu nanoparticles already in the initial state of CmZ02. As revealed by the EDX experiments on the post-MSR state, a transformation of mostly highly dispersed Cu into agglomerated Cu nanoparticles is observed for CmZ02, resembling the CmZ2 catalyst after MSR (see Fig. 3). This directly explains the almost similar identical MSR profiles in the second cycles of CmZ02 and CmZ2 (see Fig. 5).

Apart from the electron microscopic assessment of the calcined catalysts, the detailed structural evolution of metallic Cu and $ZrO_2$ as a function of the $Cu/ZrO_2$ interface dimension deserve particular

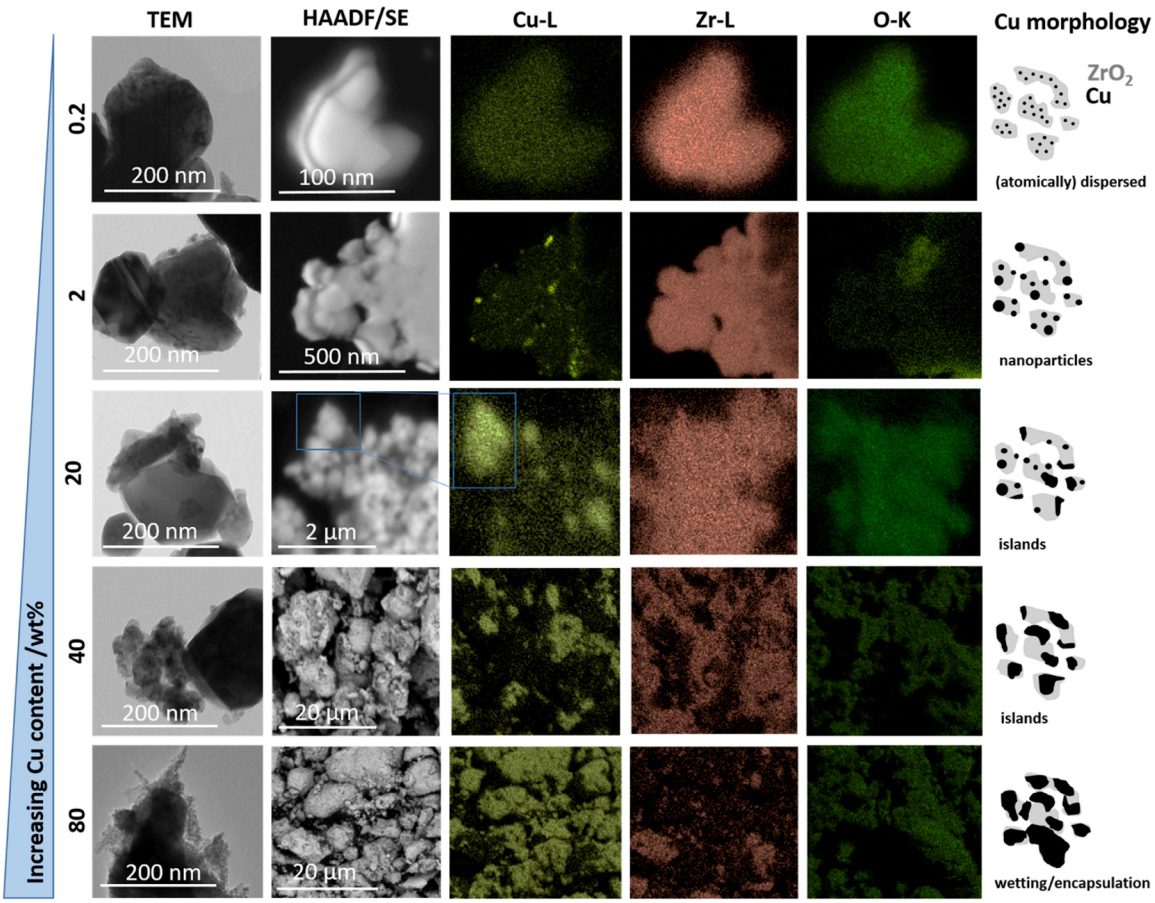


**Fig. 1.** Overview of the TEM/SEM and EDX evaluation of the Cu/$ZrO_2$ catalysts in their calcined state with increasing Cu content. From top to bottom, the Cu amount increases. The respective columns feature a representative TEM overview, HAADF (for CmZ02, CmZ2 and CmZ20) and secondary electron (SE, for CmZ40 and CmZ80) images and the characteristic Cu-L, Zr-L and O-K intensities following EDX mapping of different representative sample regions. The last column schematically highlights the transformation of the Cu morphology as a function of the Cu loading. The scale of the EDX images is identical to the HAADF or SE images.

attention – especially in view of the suspected importance of strain effects in the metallic Cu phase for high $CO_2$ selectivity [11]. We are able to provide information on the change in lattice parameter, crystallite size and microstrain as a function of Cu loading and, thus, the Cu-$ZrO_2$ interface dimension as derived from Rietveld refinement of the *ex situ* collected XRD patterns (Fig. 4). Previous work showed that the lattice parameters and unit cell volume of $ZrO_2$ decrease with Cu substitution in the $ZrO_2$ lattice [32]. However, there is no significant change in the lattice parameters and unit cell volume with increasing Cu content in our case (Panel A). We also calculated the crystallite size for all phases with (open symbols) and without (closed symbols) considering microstrain (Panel B) as a function of Cu loading. As expected, the crystallite size of all phases is slightly higher, when microstrain is considered. In essence, the crystallite size of $ZrO_2$ is no strong function of the Cu content. As expected, the crystallite sizes of the $Cu_2O$ and CuO phases increase with Cu content. The higher the Cu content, the higher the probability of Cu oxide formation. No peak broadening is observed in the XRD reflections of the metallic Cu phase, suggesting that no nano-sized crystallites are present. In contrast to the crystallite size, the determined microstrain is found to be independent of the Cu content for all phases. CuO has the highest microstrain among all samples due to its small crystallite sizes (< 20 nm), while $ZrO_2$ exhibits the smallest microstrain because it has the largest crystallite sizes.

### *3.3. Influence of the Cu-$ZrO_2$ interfacial dimensions on the catalytic methanol steam reforming performance*

To emphasize the significant effect of the addition of highly dispersed Cu (0.2 wt%) to m-$ZrO_2$, the MSR performance of CmZ02 and pure m-$ZrO_2$ are compared in Fig. 5. The profiles of the formation rate of CO are very similar, whereas the $H_2$ formation rates on CmZ02 are higher by a factor of ≈ 40 at 330 °C. Pure m-$ZrO_2$ features almost 100 % selectivity towards CO. This support-related formation of CO (onset temperature ≈ 290 °C) causes most of the carbon monoxide formed on CmZ02. However, the onset temperature of CO is ≈ 260 °C on CmZ02, suggesting the creation of an additional low-temperature reaction pathway toward CO requiring the presence of Cu. This already indicates that the suppression of this support-related selectivity-spoiling activity toward CO is crucial for high $CO_2$ selectivity.

The MSR performance of CmZ02 in the first two catalytic cycles is visualized once more in Fig. 6, Panel A to enable direct comparison with CmZ2 in Panel B. The first and the second MSR run differ considerably, supporting the changes observed with electron microscopy (see Fig. 3). During the 1$^{st}$ cycle, the $H_2$ and $CO_2$ formation rates exhibit an extremely steep increase and cannot be fitted by an Arrhenius equation utilizing physically meaningful parameters, suggesting ongoing activation of the catalyst at the MSR onset temperature. This effect is explained by the incorporation of Cu into the $ZrO_2$ lattice, which also accounts for the invisibility of Cu in TGA and XRD. The observations are similar to those attributed to formation of a ternary Cu-Zr-O oxide phase as described by Tada et al. [33] for a Cu/amorphous $ZrO_2$ system. The maximum activity in this study is also lowered, hinting at deactivation by Cu sintering as indicated by XPS and electron microscopy investigations after catalysis (see Table 4 and Fig. 3). The $CO_2$ selectivity, the methanol conversion and the CO-TOF essentially remain the same.

The MSR profile of CmZ2 (Fig. 6 Panel B) does not show the steep

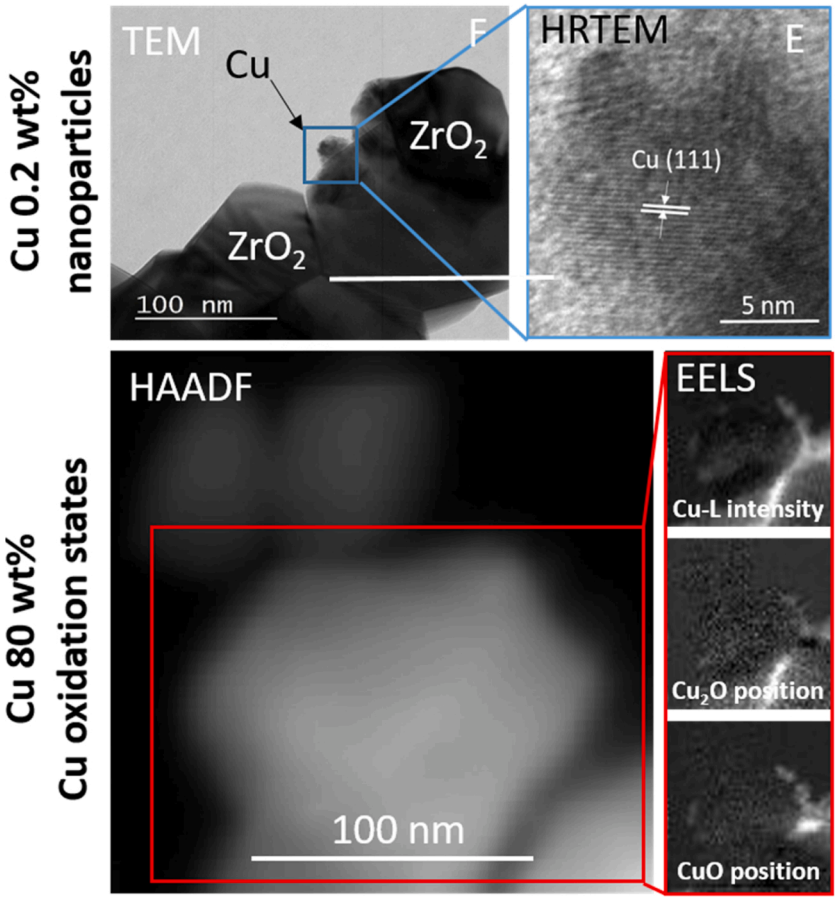


**Fig. 2.** Top panel: TEM and HRTEM image of a single Cu particle decorating a m-$ZrO_2$ grain featuring atomically resolved Cu(111) lattice fringes on CmZ02 after calcination. Bottom panel: HAADF and EELS mapping images of a representative region on CmZ80 after calcination. For the EEL spectrum images, the total Cu-L intensity is shown alongside images using the fraction of electrons with a characteristic energy loss for electrons stemming from CuO and $Cu_2O$.

increase in the $H_2$ and $CO_2$ formation rates in the first cycle and the MSR reaction onset is observed already at ≈ 200 °C. The general characteristics of the catalytic profiles of CmZ02 and CmZ2 in the second cycle are almost identical except for small shifts in the onset temperatures. In contrast to CmZ02, however, the TOFs of CmZ2 including the methanol conversion are increased in the second cycle, suggesting further activation of the catalyst. Up to 270 °C (250 °C in the second cycle), the catalyst exhibits almost 100 % $CO_2$ selectivity, which is a common feature of all investigated samples. A striking feature of both catalysts with the lowest Cu loading is the pronounced activation between the first and the second cycle. For CmZ02, we ascribe this to the decomposition of the ternary Cu-O-Zr oxide in the first cycle (*cf.* Fig. 3) and the appearance of small Cu particles. In the second MSR cycle, we tentatively assign the further activation to an increased number of those formed Cu nanoparticles. We hence assume that partial activation occurs during both the first and the second cycle. For CmZ2, small Cu particles were present even before the first cycle, explaining the earlier onset of reaction. We ascribe the further activation from the first to the second cycle to the slight agglomeration of Cu particles to an optimized Cu//$ZrO_2$ interface for MSR (which at the end of the first cycle/during the second cycle apparently is similar to CmZ02 derived from the almost perfect match of the catalytic MSR traces and the similar TEM data). A similar reasoning applies for CmZ20, which also exhibits an increase in activity form the first to the second MSR cycle.

A short note on the use of TOF values for CmZ02 and CmZ2 should be added. We deliberately used the number of accessible Cu atoms as derived from $N_2O$ adsorption experiments as a measure for TOF calculation, although the catalysts activate between the first and the second cycle. We take this as a reasonable approximation to internally compare the activity trend between the catalysts with different Cu loadings.

The methanol steam reforming profiles of CmZ20 in Fig. 7 Panel A depict different characteristics compared to CmZ2 and CmZ02. Although the onset temperatures of $H_2$ and $CO_2$ formation are very similar to the ones of CmZ2, the activation from the first and the second cycle is much less pronounced. The onset temperature of CO, however, is decreased from ≈ 260 °C (CmZ2) to ≈ 220 °C in CmZ20, which narrows the temperature regime of > 90 % $CO_2$ selectivity.

The trend of lower $CO_2$ onset temperatures continues with CmZ40 in Fig. 7 Panel B, where $H_2$ and $CO_2$ start to be formed around 160 °C and 180 °C. Additionally, the onset of CO is lowered to around 200 °C. The profiles of the two MSR cycles are almost identical and the overall appearance is similar to CmZ20.

The two MSR cycles of CmZ80 match each other, indicating that no additional activation occurs, and the onset temperatures of $H_2$ and $CO_2$ are located at ≈ 130 °C (see Fig. 8). Several features of this sample are distinct. The onset of CO formation increases once more to ≈ 220 °C compared to 190 °C on CmZ40. This expands the temperature regime of > 90 % $CO_2$ selectivity and the maximum TOFs of $H_2$ and $CO_2$ are located around the onset of CO formation.

As the attentive reader will have noticed, the samples CmZ02, CmZ2, CmZ20 and CmZ40 all display reproducible non-MSR related $CO_2$ formation in both catalytic cycles (except CmZ02 in the first cycle), reflected in the absence of concomitant $H_2$ formation. Rather, this particular $CO_2$ formation starts at lower temperatures and is superimposed on the $CO_2$ arising from MSR at its reaction onset. Since this effect is neither visible on CmZ80 (see Fig. 8) nor pure m-$ZrO_2$ (see Fig. 5) and its extent decreases slightly with increasing Cu loading up to 40 wt%, it can be ascribed to a cooperative operation of Cu and $ZrO_2$.

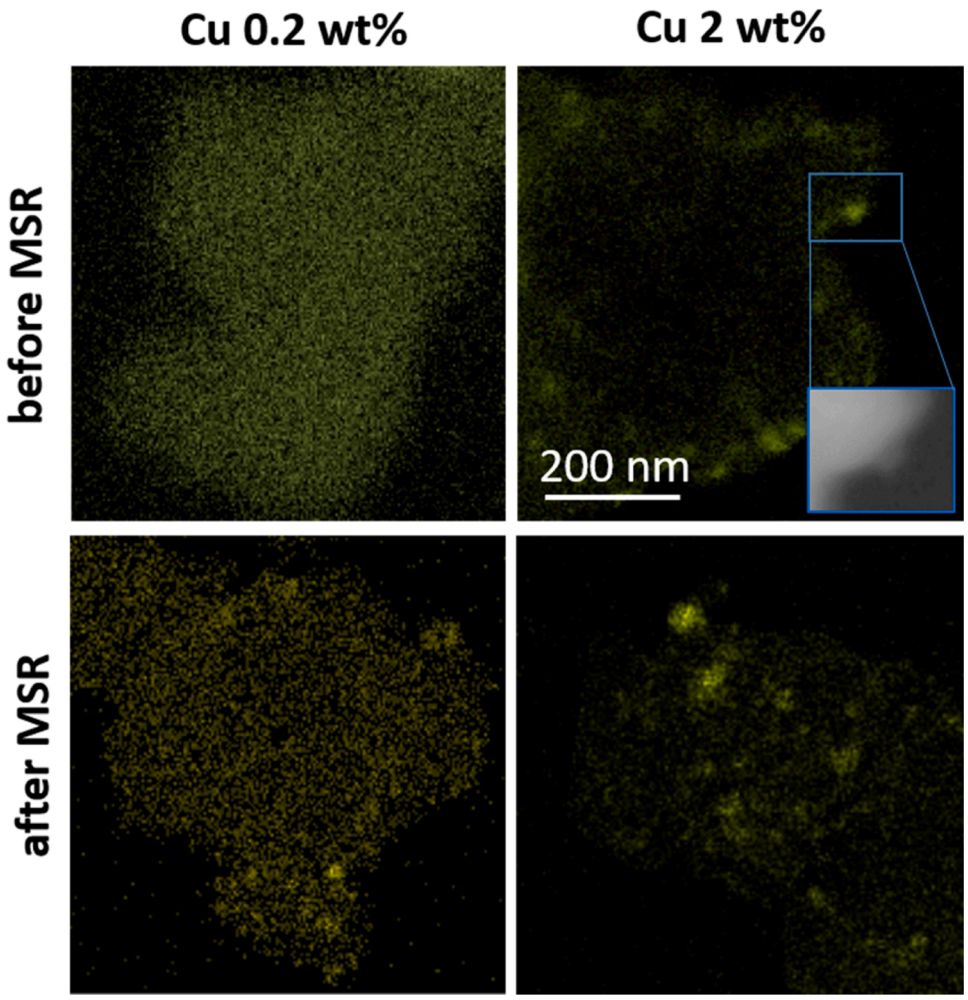


**Fig. 3.** TEM EDX maps showing the Cu-L intensities of CmZ02 and CmZ2 before and in the post-MSR state to document the evolution of the Cu nanoparticles during MSR for the catalysts with the lowest Cu loadings.

This is in good agreement with the TEM results, where wetting and encapsulation of the support by Cu is visible on CmZ80 (see Fig. 1), reducing the accessible Cu-$ZrO_2$ interface sites. There are two possible explanations for this non-MSR-related $CO_2$ formation. The first one is based on a redox reaction of Cu oxide species at the Cu-$ZrO_2$ interface and methanol, yielding $CO_2$, water and metallic Cu. This phase boundary oxide could be formed upon introduction of the MSR mixture at 100 °C after the pre-reduction. This theory is supported by observations of Werner et al. on a Cu foil that was pre-dosed with $O_2$, where $CO_2$ formation from methanol was detected around 200 °C [34]. The other potential explanation revolves around storing $CO_2$ stemming from previous treatments/MSR cycles. Upon heating, the stored $CO_2$ (presumably present as (bi-) carbonates that decompose at elevated temperatures) is re-released again as additional $CO_2$ between 120 °C and 250 °C. The temperature range of carbonate decomposition fits the reported values of Pokrovski et al., who observed the formation of ionic and bidentate bicarbonates as well as mono- and bidentate carbonates upon exposure of m-$ZrO_2$ to $CO_2$. Starting at 25 °C, desorption/decomposition of bicarbonates with a maximum rate at around 130 °C and further decomposition of carbonates between 180 °C and 380 °C occurs [35].

In conclusion, with increasing surface-wetting (blocking) of the support (reflected by the increase in Cu loading), several trends for MSR operation are observed (visualized in Fig. 9 and summarized in Table 3). Firstly, the onset temperatures of $CO_2$ and $H_2$ decrease. Secondly, the TOFs of $CO_2$ and $H_2$ at 220 °C increase. The onset temperature of CO passes through a minimum on CmZ40 and the difference between the first and the second MSR cycle is generally less pronounced.

### *3.4. Development of the surface atomic Cu/Zr ratio as a function of the Cu-$ZrO_2$ interface: X-ray photoelectron spectroscopy*

The spectra of the Cu 2p and Cu LMM regions are depicted in Fig. S2 in the SI. Since the measurements were conducted *ex situ* with intermediate exposure to air, the spectra are not clearly representative of the post-MSR state anymore. Hence, no conclusions regarding the influence of the copper loading on the pre- and post-MSR surface oxidation state of Cu could be drawn. However, the atomic ratio of Cu and Zr at the catalyst surface was calculated (Table 4) and continuously increases with increasing copper loading after calcination, confirming the trends observed by microscopy and dissociative $N_2O$ adsorption. Another consequence of this trend is the concomitant decrease in the exposed m-$ZrO_2$ surface area, which implies that the extent of support-related effects should decrease with increasing Cu loading in MSR. Furthermore, the Cu/Zr ratio decreases after MSR for all samples but CmZ2, indicating slight sintering of metallic Cu during MSR. Relating the XPS data to the TEM investigations, we note that also the Cu/Zr ratios indicate considerable wetting of $ZrO_2$ by Cu, although not by 100 %. The situation for the CmZ80 catalyst is reminiscent of a “Raney-Cu catalyst”, with residual patches of oxide. In fact, a broad patent literature for Raney-type Cu catalysts is available, with the residual oxide component (typically interfacial $Al_2O_3$) serving the purpose to keep the strongly predominant

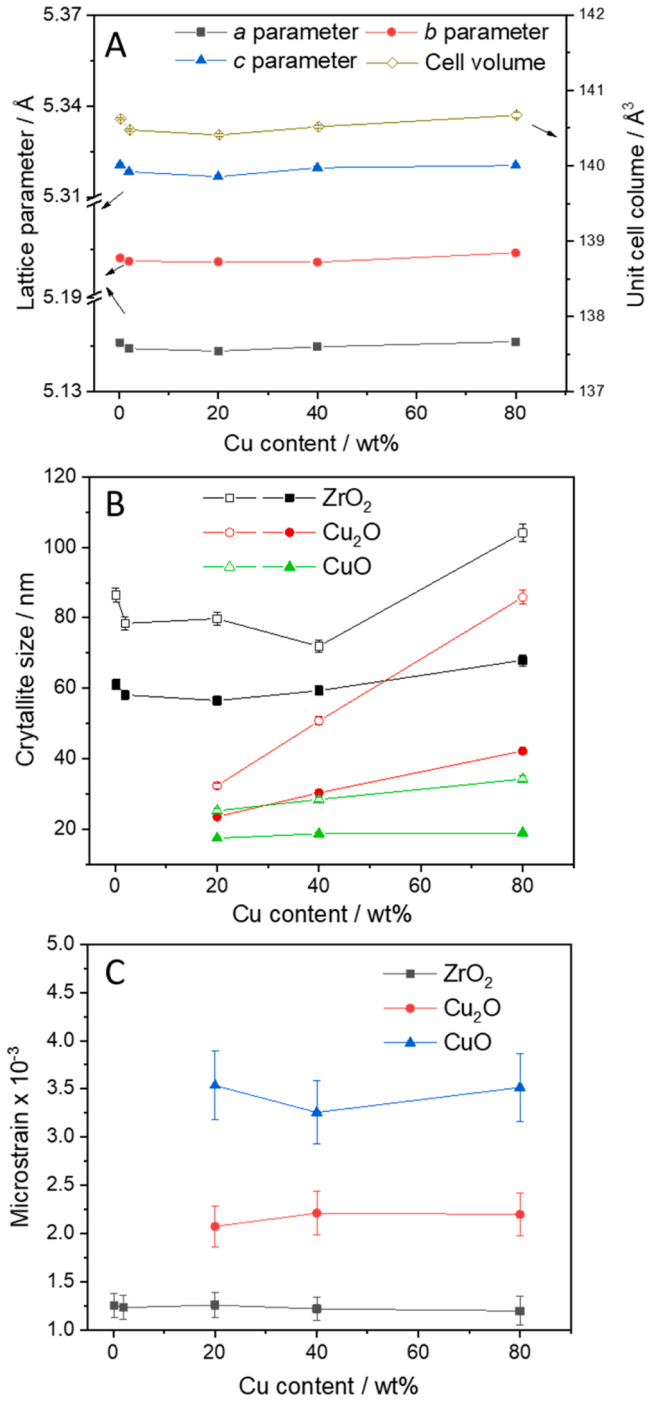


**Fig. 4.** Development of $ZrO_2$ lattice parameters/unit cell volume (Panel A), crystallite size (Panel B) and microstrain (Panel C) as a function of Cu loading and, therefore, $Cu/ZrO_2$ interface dimension, as derived from Rietveld refinement of the *ex situ* collected XRD data. Lines drawn as a guide to the eye.

metal phase dispersed.

The determination of the specific Cu surface area *via* dissociative $N_2O$ adsorption over a loading range from 0.2 wt% to 80 wt% Cu imposes certain necessary assumptions on the calculation of the TOF values. The redox chemistry of highly dispersed Cu with a high metal-support interface area (CmZ02) differs from the bulk-like support-wetting Cu phase in CmZ80. Thus, the restriction of only surface oxidation of metallic Cu to $Cu_2O$ cannot be upheld. The embedded hemispherical particle approximation is also not valid anymore in CmZ80, which would make the estimation of the average particle size less reliable.

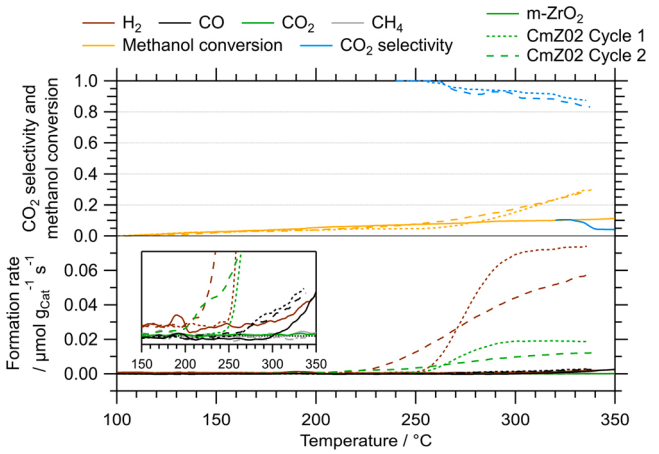


**Fig. 5.** MSR profiles of CmZ02 and pure m-$ZrO_2$ between 100 °C and 350 °C. The traces are shown up to a maximum methanol conversion of 30 %. Upper panel: orange – methanol conversion, blue –$CO_2$ selectivity; lower panel: Formation rates of brown – $H_2$, green –$CO_2$, black –CO, gray –$CH_4$. Dashed lines refer to CmZ02. The inset represents a zoomed region highlighting the performance of pure m-$ZrO_2$. Heating rate: 5 °C $min^{-1}$. Sample mass: CmZ02 – 78.0 mg; m-$ZrO_2$ – 82.2 mg.

To circumvent these deficiencies and to corroborate the values of the $SA_{Cu}(N_2O)$ obtained by dissociative $N_2O$ adsorption, the Cu/Zr atomic surface ratio from XPS was utilized in combination with the BET-determined specific catalyst surface area. Based on the Cu/Zr ratio, the $SA_{Cu}$(XPS) was estimated by multiplication of the BET surface area with the near-surface atomic Cu percentage (based on the Cu 2p and Zr 3d regions) from XPS. A comparison of the Cu surface areas determined from $N_2O$ dissociation and XPS, $SA_{Cu}(N_2O)$ and $SA_{Cu}$(XPS), respectively, is given in Table 4. The general trend considering only CmZ02 and CmZ80 is reflected in both values, while the continuity of the increase present in $SA_{Cu}(N_2O)$ is not visible in $SA_{Cu}$(XPS). However, as dissociative $N_2O$ adsorption requires the presence of Cu in its metallic form, the catalysts have to be pre-reduced for these experiments, which might involve unavoidable sintering of Cu particles. The BET surface area of the catalysts was measured in the state after calcination, which is why the estimation of $SA_{Cu}$(XPS) was only conducted for the calcined state. The BET surface area could be altered upon MSR and the involved pre-treatments. Additionally, the Cu/Zr surface ratio after MSR and the involved pre-treatments is lower for all samples except for CmZ2, inferring that Cu particle sintering occurs. However, considering the Cu/Zr surface ratio after MSR in combination with the BET surface area after calcination yields more comparable values for $SA_{Cu}(N_2O)$ and $SA_{Cu}$(XPS). Even more importantly, the trends in the continuous increase of the TOFs of $H_2$ and $CO_2$ at 220 °C in MSR calculated with either $SA_{Cu}(N_2O)$ or $SA_{Cu}$(XPS) are similar (see Table 3).

### 3.5. Redox behavior of the $Cu/ZrO_2$ catalysts: in situ thermogravimetry

The redox behavior of each sample in an oxidation-reduction-oxidation cycle was investigated to characterize the kinetics of oxidation/reduction and to further confirm the copper loading. The pre-oxidation as well as the re-oxidation are discussed in the SI Section D. The number of signals observed in the reduction of Cu-based catalysts in MSR has been reported to deliver information on the interaction of Cu with the support [36]. Liu et al. [37] describe the reduction behavior of $Cu/ZrO_2$ catalysts with two signals, where they relate the low-temperature feature to copper species strongly interacting with the support and the high-temperature peak to bulk CuO-like copper species.

The reduction in hydrogen up to 300 °C does not show any change of the mass for the m-$ZrO_2$ reference sample (see Fig. 10). The TPR treatment yields a single reduction signal for all catalysts, including the CuO

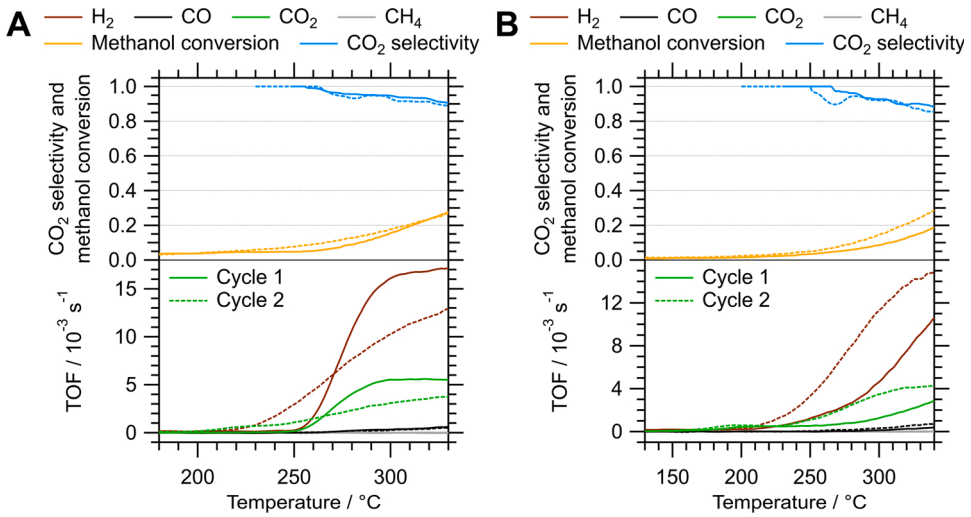


**Fig. 6.** MSR profiles of CmZ02 between 180 °C and 330 °C (Panel A) and CmZ2 between 130 °C and 340 °C (Panel B). The traces are shown up to a maximum methanol conversion of 30 %. Upper panel: orange – methanol conversion, blue –$CO_2$ selectivity; lower panel: TOF of brown – $H_2$, green –$CO_2$, black –CO, gray –$CH_4$. Dashed lines indicate traces of the second cycle. Heating rate: 5 °C $min^{-1}$. Sample mass: CmZ02 – 78.0 mg; CmZ2 – 64.0 mg.

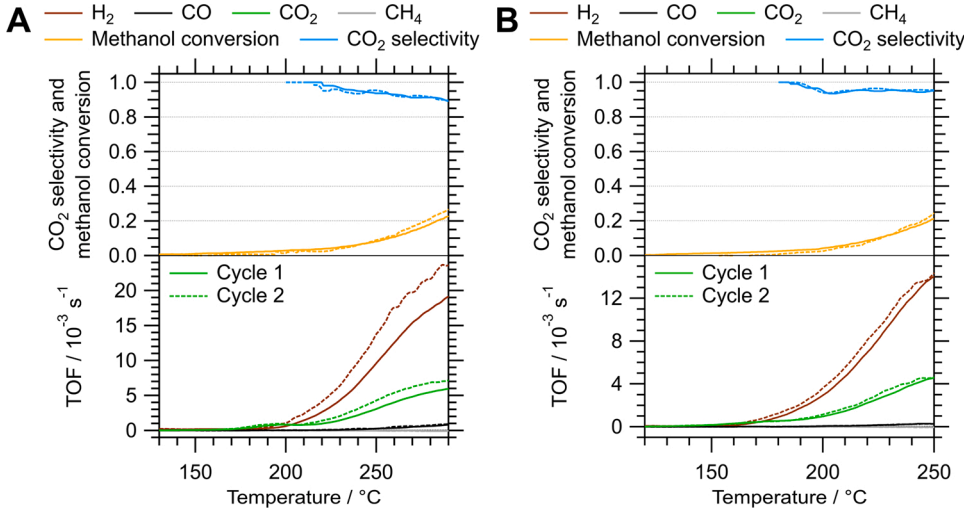


**Fig. 7.** MSR profiles of CmZ20 between 130 °C and 290 °C (Panel A) and CmZ40 between 120 °C and 250 °C (Panel B). The traces are shown up to a maximum methanol conversion of 30 %. Upper panel: orange – methanol conversion, blue –$CO_2$ selectivity; lower panel: TOF of brown – $H_2$, green –$CO_2$, black –CO, gray –$CH_4$. Dashed lines indicate traces of the second cycle. Heating rate: 5 °C $min^{-1}$. Sample mass: CmZ20 – 65.0 mg; CmZ40 – 88.6 mg.

reference material. The exception is CmZ02, since the sensitivity of the TGA measurements is too low to detect any significant mass loss upon reduction in hydrogen as well as in the re-oxidation afterwards (see SI Fig. S4). The signal temperatures, given in Table 5, are very similar, but tend to increase with higher copper loading. The signal of CmZ80 is shifted to lower values relative to CmZ40, suggesting a more pronounced reducibility of CmZ80. The reduction onset temperature for a CuO reference sample is slightly higher than for the catalysts supported on zirconia, which suggests a synergistic effect of $ZrO_2$ in the reduction of the copper phase, potentially by supplying an active phase boundary for hydrogen activation. In addition, the reduction signal areas serve as a measure for the copper loading (see Table 5), which agrees well with the results from XRD, as well as ICP-OES.

In contrast to the reports of Ritzkopf et al. [15], Köppel et al. [36] and Liu et al. [37], only one broad signal is observed in the TPR profiles of the catalysts in this study. The signal temperatures of the profiles increase continuously with the exception being CmZ80, whereas the onset temperatures of all samples lie around 180 °C. The shift of the signal temperatures is induced by kinetic effects due to the different particle sizes of copper in the catalysts. The onset temperature of pure CuO, however, is located at approximately 200 °C, suggesting the occurrence of a synergistic effect of $ZrO_2$ for the reduction of the copper phase in all samples.

### 3.6. *Dynamical response of the Cu bulk oxidation state during methanol steam reforming: in situ X-ray diffraction*

We investigated the bulk structural changes of the copper phase to elucidate the role of oxidized bulk Cu species on the catalytic performance in MSR. We also discuss the dynamical behavior of the bulk Cu oxidation state during the oxidative and reductive pre-treatments in this section (experiments not shown, except for CmZ02, see SI Fig. S6).

Due to the detection limit of XRD, no copper phase can be observed in CmZ02 during the pre-reduction (see SI Fig. S6), even though the loading was confirmed by ICP-OES (see Table 1). However, this does not exclude the presence of copper in an amorphous form or the incorporation of Cu into the zirconia lattice resulting in a ternary oxide, as reported for $Cu/ZrO_2$ catalysts [33]. The *in situ* XRD patterns of CmZ2 and

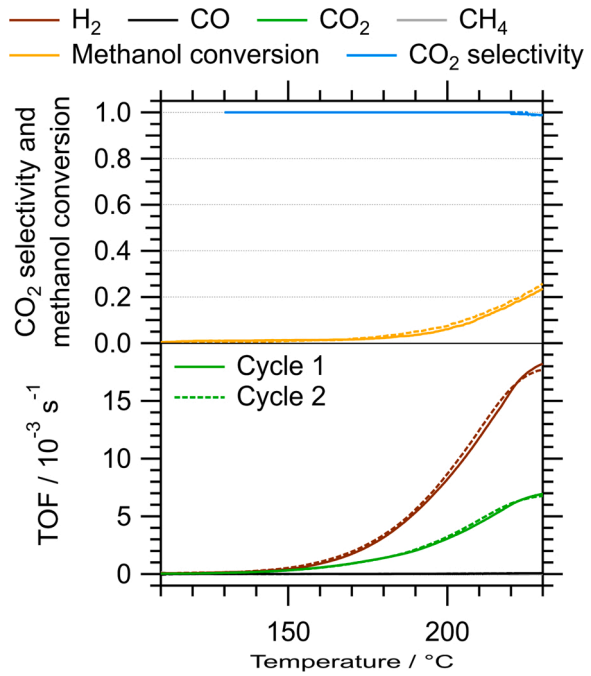


**Fig. 8.** MSR profiles of CmZ80 between 110 °C and 230 °C. The traces are shown up to a maximum methanol conversion of 30 %. Upper panel: orange – methanol conversion, blue −$CO_2$ selectivity; lower panel: TOF of brown – $H_2$, green −$CO_2$, black −CO, gray −$CH_4$. Dashed lines indicate traces of the second cycle. Heating rate: 5 °C $min^{-1}$. Sample mass: 86.6 mg.

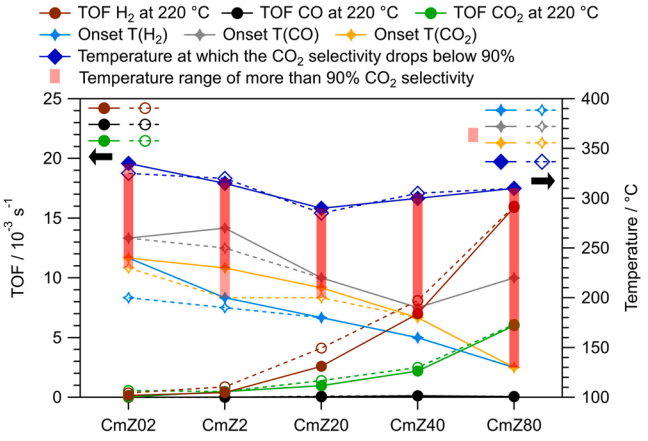


**Fig. 9.** Visualization of the key catalytic parameters of all studied Cu/m-$ZrO_2$ samples. The TOFs at 220 °C are compared on the left axis and the onset temperatures are given on the right axis. The data of the first cycle is depicted with filled markers and solid lines, whereas the information on the second cycle is shown with hollow markers and dashed lines. The temperature at which the $CO_2$ selectivity decreases below 90 % is illustrated in dark blue and the resulting temperature region of > 90 % $CO_2$ selectivity is highlighted with a semi-transparent red bar, where the congruency of the first and second cycle is visible as a more saturated color. Lines have been drawn as a guide to the eye.

CmZ20 collected during MSR are also presented in the SI, since no intermediate formation of $Cu_2O$ or CuO was observed (see SI Figs. S7 and S8, respectively).

In CmZ2, only 0.5 wt% of $Cu_2O$ is detected as the only copper phase after calcination (see SI Table 1 and Fig. S5). The remaining fraction must be present in an X-ray amorphous state or in phases below the technique's detection limit, since both ICP-OES and TGA measurements confirmed the copper loading (2 wt%). The remaining Cu could be present in the form of an amorphous ternary oxide similar to the one in

**Table 3**
Summary of key catalytic parameters.

| | CmZ02 | CmZ2 | CmZ20 | CmZ40 | CmZ80 |
|---|---|---|---|---|---|
| $E_a$ $CO_2$ / kJ $mol^{-1}$ | 103[a] | 110 | 96 | 92 | 85 |
| | 102 | 101 | 93 | 91 | 85 |
| $E_a$ CO / kJ $mol^{-1}$ | 108 | 121 | 107 | 103 | 107 |
| | 115 | 113 | 105 | 103 | 105 |
| Onset T($H_2$) / °C | 240 | 200 | 180 | 160 | 130 |
| | 200 | 190 | 180 | 160 | 130 |
| Onset T(CO) / °C | 260 | 270 | 220 | 190 | 220 |
| | 260 | 250 | 220 | 190 | 220 |
| Onset T ($CO_2$) / °C | 240 | 150[b], 230 | 150[b], 210 | 120[b], 180 | 130 |
| | 200[b], 230 | 150[b], 200 | 150[b], 200 | 120[b], 180 | 130 |
| T(> 90 % $CO_2$) / °C | 240–335 | 150–315[c] | 150–290[c] | 120–300[c, e] | 130–310[e] |
| | | 200–315[d] | 210–290[d] | 180–300[d, e] | |
| | 200–325[c] | 150–320[c] | 150–285[c] | 120–305[c, e] | 130–310[e] |
| | 230–325[d] | 230–320[d] | 200–285[d] | 180–305[d, e] | |
| TOF($N_2O$) $H_2$ at 220 °C / $10^{-3}$ $s^{-1}$ | 0.15 | 0.39 | 2.6 | 7.0 | 15.9 |
| | 0.37 | 0.87 | 4.12 | 8.1 | 16.0 |
| TOF(XPS) $H_2$ at 220 °C / $10^{-3}$ $s^{-1}$ | 0.049 | 0.059 | 0.32 | 2.3 | 7.6 |
| | 0.12 | 0.13 | 0.49 | 2.7 | 7.7 |
| TOF($N_2O$) $CO_2$ at 220 °C / $10^{-3}$ $s^{-1}$ | 0.023 | 0.48 | 0.97 | 2.2 | 6.0 |
| | 0.57 | 0.48 | 1.4 | 2.5 | 6.1 |
| TOF(XPS) $CO_2$ at 220 °C / $10^{-3}$ $s^{-1}$ | 0.0077 | 0.074 | 0.12 | 0.74 | 2.9 |
| | 0.19 | 0.073 | 0.17 | 0.84 | 2.9 |

$E_a$ = apparent activation energy obtained by fitting the Arrhenius equation to the experimental TOF values with the first and the second cycle given vertically adjacent for comparability.

[a] no Arrhenius behavior, therefore unreliable.

[b] non-MSR-related $CO_2$ formation starts at this temperature, onset temperature for catalytic $CO_2$ formation is estimated below.

[c] including the non-MSR-related $CO_2$ formation.

[d] neglecting the non-MSR-related $CO_2$ formation.

[e] upper temperature limit above of the depicted traces, but shown for completeness of the parameters; TOF($N_2O$) = TOFs obtained with the $SA_{Cu}$ determined *via* dissociative $N_2O$ adsorption; TOF(XPS) = TOFs obtained with the $SA_{Cu}$ based on the surface atomic Cu/Zr ratio from XPS and the specific catalyst surface area from BET.

CmZ02, where this value could be interpreted as the limit for Cu incorporation into this specific $ZrO_2$ phase accompanied by the presence of crystalline Cu. During pre-reduction, $Cu_2O$ is transformed into metallic Cu, leading to the formation of a stable amount of about 1.2 wt % of metallic Cu during MSR. (SI Fig. S7).

After calcination of CmZ20, metallic Cu next to $Cu_2O$ and CuO is observed (SI Fig. S5. Several Cu oxide phases are obtained during the pre-oxidation step after 10 min at 400 °C in $O_2$. The final composition is a mixture of 6.5 wt% $Cu_2O$, 17.0 wt% CuO and 76.4 wt% m-$ZrO_2$. Pre-reduction quantitatively converts the Cu oxide phases to metallic Cu (19.9 wt%), which remains stable during MSR (Fig. S8).

For CmZ40, the calcination in air at 400 °C for 2 h results in the formation of metallic Cu, $Cu_2O$ and CuO (SI Fig. S5). After pre-oxidation, metallic Cu does not disappear completely and the final composition is 0.8 wt% Cu, 11.6 wt% $Cu_2O$, 32.1 wt% CuO and 55.5 wt% m-$ZrO_2$. Pre-reduction yields metallic Cu as the predominant phase with a final composition of 39.6 wt% Cu°, 0.4 wt% $Cu_2O$ and 60.0 wt% m-$ZrO_2$, which is in excellent agreement with the nominal loading as well as with the data from ICP-OES and TGA. During MSR, traces of $Cu_2O$ are already present at the beginning at 120 °C (approximately 0.8 wt%, see Fig. 11 Panels A and B). Above 170 °C, Cu° is continuously oxidized to $Cu_2O$,

**Table 4**
Atomic surface ratio of Cu and Zr according to XPS after calcination and after MSR and a comparison of differently obtained $SA_{Cu}$ values.

| | | CmZ02 | CmZ2 | CmZ20 | CmZ40 | CmZ80 |
|---|---|---|---|---|---|---|
| Atomic Cu/Zr ratio | After calcination | 0.2 | 0.6 | 1.0 | 1.1 | 6.2 |
| | After MSR350 | 0.1 | 0.7 | 0.5 | 0.8 | 3.5 |
| Comparison of Cu surface area values | $SA_{Cu}(N_2O)$[*1] / $m^2\ g_{Cat}^{-1}$ | 0.18 | 0.23 | 0.24 | 0.35 | 0.41 |
| | $SA_{Cu}(XPS)$[*2] / $m^2\ g_{Cat}^{-1}$ | 0.5 | 1.5 | 2.0 | 1.0 | 0.9 |

[*1] the presence of metallic copper is a prerequisite, hence, the samples were pre-reduced in $H_2$ at 300 °C.
[*2] the BET surface area and the Cu/Zr atomic surface ratio were obtained in the calcined state, which explains why they are consistently larger than the corresponding $SA_{Cu}(N_2O)$ values.

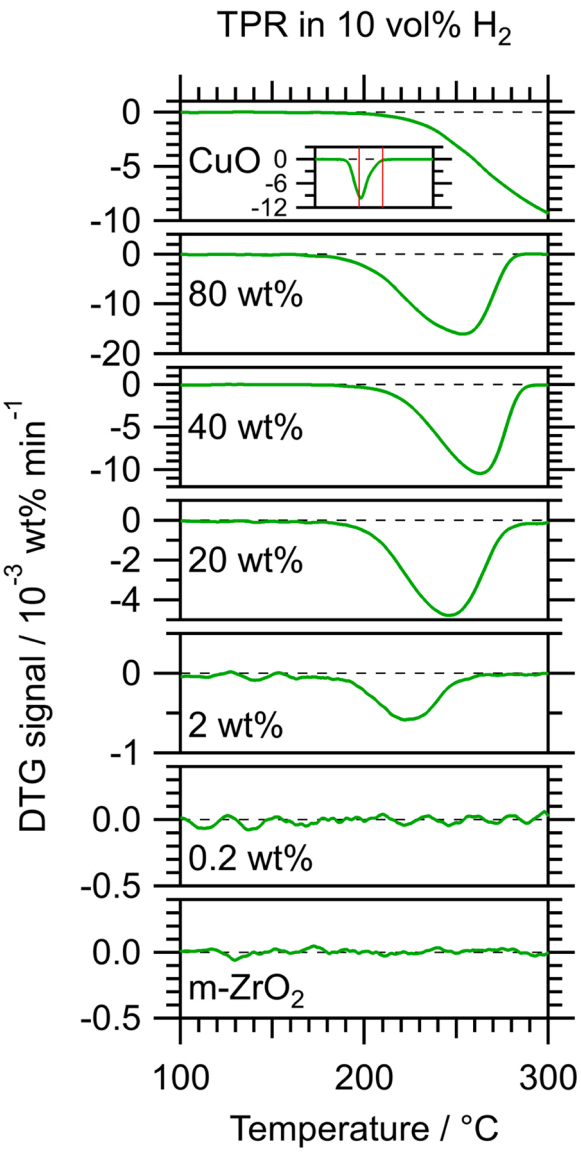


**Fig. 10.** DTG profiles of the TPR treatment in 10 vol% $H_2$ up to 300 °C. The five samples, denoted by their nominal copper loading, including the two pure reference materials, m-$ZrO_2$ and CuO, are depicted. The inset in the CuO panel shows the full profile including the isothermal and the cooling period, where the two red lines separate the three regions of the temperature cycle (heating, isothermal, cooling).

reaching its maximum at the beginning of the isothermal period with a weight fraction of 27 wt%. Only traces of $Cu_2O$ remain during the isothermal period (≈ 0.3 wt%, Fig. 11 Panels A and C) due to the increased reduction potential of the MSR reaction mixture at higher methanol conversions at high temperatures. The rest of Cu is re-

**Table 5**
Summary of the TGA results.

| Sample name | Copper loading from TGA (reduced state) / wt% | Reduction signal temperature / °C | Re-oxidation signal temperature / °C* | Re-oxidation signal area / %* |
|---|---|---|---|---|
| CmZ02 | -[a] | -[a] | -[a] | -[a] |
| CmZ2 | 1.8 | 225 | 160, 290 | 44, 56 |
| CmZ20 | 19 | 245 | 170, 245, 365 | 31, 25, 44 |
| CmZ40 | 38 | 265 | 170, 225, 345, 435 | 25, 15, 42, 18 |
| CmZ80 | 79 | 255 | 180, 245, 360, 500 | 30, 3, 43, 24 |
| CuO | 99 | 300 | 235, 355, 430, 535 | 22, 22, 8, 48 |

[a] not detectable with TGA.
* Experiments discussed and shown in the SI, Section D.

transformed to the metallic state.

Similar to CmZ40, CmZ80 exhibits a mixture of 9.9 wt% Cu, 44.7 wt% $Cu_2O$, 27.6 wt% CuO and 17.8 wt% m-$ZrO_2$. After pre-oxidation and pre-reduction, the sample is composed of 80.5 wt% metallic Cu and 19.5 wt% m-$ZrO_2$. Intermediate formation of $Cu_2O$ (up to 0.8 wt% at 190 °C, Fig. 12 Panels A and B) occurs during MSR. $Cu_2O$ decomposes at 240 °C, coinciding with the region of close to 100 % $CO_2$ selectivity and metallic Cu remains stable during the isothermal period (Fig. 12 Panels A and C).

Several points that distinguish the phase evolution of the samples during MSR operation are important. No crystalline copper phases are visible in CmZ02, although Cu is present in the sample as revealed by other characterization techniques such as ICP, TEM-EDX and XPS. CmZ2 and CmZ20 behave similarly and do not feature formation of crystalline $Cu_2O$ or CuO. A stable concentration of metallic copper is observable during MSR. Both CmZ40 and CmZ80 display intermediary formation of $Cu_2O$ during MSR operation. The selective intermediary oxidation of Cu° to $Cu^+$ in both CmZ40 and CmZ80 has already been correlated with an enhanced methanol reforming performance of Cu-based catalysts. Oguchi et al. observed the formation of $Cu_2O$ in the MSR mixture at 250 °C on a Cu/$ZrO_2$ (80 wt% CuO) catalyst, displaying a superior performance compared to an analogous Cu/$CeO_2$ system [13,18]. Agrell et al. observed the formation of a stable $Cu^+$ species on a pre-reduced Cu/ZnO/$ZrO_2$/$Al_2O_3$ during preferential oxidation of methanol [7]. Raimondi et al. [17] inferred a temperature dependency of the Cu oxidation state in POM. $Cu^+$ species were detected after exposure to the reaction mixture below 237 °C and re-formation of metallic Cu above 257 °C. This upper temperature limit resembles the re-reduction temperature to the metallic Cu phase in CmZ80.

We also focused upon the associated structural changes involving lattice parameter or microstrain variation during reduction and/or MSR operation for all samples and the CmZ80 sample as the catalytically most promising one in particular. After pre-reduction and at different conditions during MSR operation, the lattice parameters of $ZrO_2$ and metallic Cu monitored by *in situ* XRD only feature the expected thermal lattice expansion during heating, but no strong change in lattice parameter, crystallite size or microstrain for any Cu loading is observed. We might therefore infer that albeit the dimensions of the Cu/$ZrO_2$ interface vary

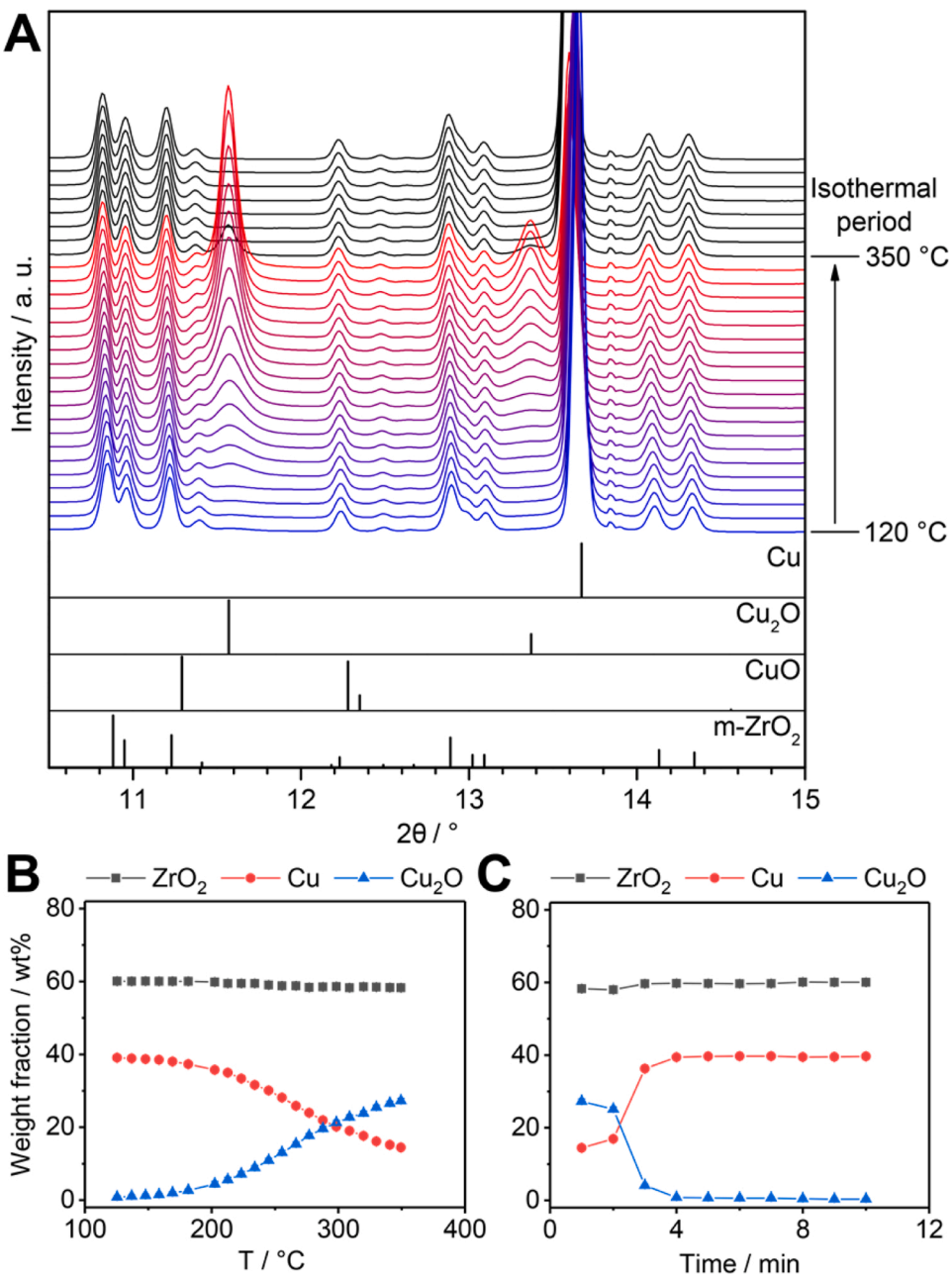


**Fig. 11.** Panel A: *In situ* X-ray diffraction (XRD) measurement of CmZ40 in the MSR mixture from 120 °C - 350 °C at 25 keV beam energy ($\lambda$ = 0.4982 Å). The temperature evolution is color-coded with the heating period as a gradient from blue to red with the isothermal period in black. The references at the bottom of all depicted *in situ* XRD graphs were taken from ICDD database [21] entries and relate the reflections to the different structures, namely m-$ZrO_2$ (PDF card #00-037-1484) [38], Cu (PDF card #00-004-0836) [39], CuO (PDF card #00-045-0937) [40] and $Cu_2O$ (PDF card #00-005-0667) [41]. Panels B and C: Composition of the sample during the heating period and the isothermal phase according to RR.

strongly as a function of Cu loading, the interface itself exhibits a high structural stability and a more or less unstrained state irrespective of Cu loading. As these features remain stable even during reduction or MSR operation, a predominant and single direct influence on $CO_2$ selectivity appears unlikely.

### 3.7. Discussion of the results

The variation of the copper loading in Cu/m-$ZrO_2$ catalysts from 0.2 wt% to 80 wt% results in a drastically different dispersion of the Cu phase accompanied by a distinct catalyst morphology. Even though dissociative $N_2O$ adsorption reveals a similar specific copper surface area for all catalysts, the values for the Cu dispersion range from 18 % (CmZ02) to 0.09 % (CmZ80). The general validity of these values is confirmed by estimation of the $SA_{Cu}$ utilizing the Cu/Zr atomic surface ratio determined by XPS and the specific BET catalyst surface area. This directly reflects the morphology as demonstrated by electron microscopy, where the Cu distribution varies from highly dispersed (CmZ02) over formation of larger particles (CmZ2) and islands (CmZ20, CmZ40) to wetting and encapsulation of $ZrO_2$ (CmZ80). A decrease of the Cu/Zr ratio atomic surface ratio after MSR indicates sintering of Cu. However, a clear correlation of the oxidation state of Cu or the degree of the decrease of the Cu/Zr ratio at the catalyst surface is not obvious.

TGA investigations indicate a similar reduction behavior for all catalysts with only slight shifts of the reduction peak temperatures. The presence of only one reduction peak points to the presence of merely one Cu (oxide) species, as additional peaks can be ascribed to a separation of bulk-like Cu and Cu strongly interacting with the support [15,36]. *In situ* XRD studies reveal a distinct intermediary bulk oxidation of the Cu phase during MSR in CmZ40 and CmZ80, while only metallic Cu can be observed in CmZ2 and CmZ20 (Cu in CmZ02 not visible). The amount of bulk $Cu_2O$ formed is considerably different for the two catalysts, where up to 27 wt% are visible in CmZ40 in contrast to only 0.8 wt% in CmZ80. Since CmZ40 and especially CmZ80 exhibit the best performance in

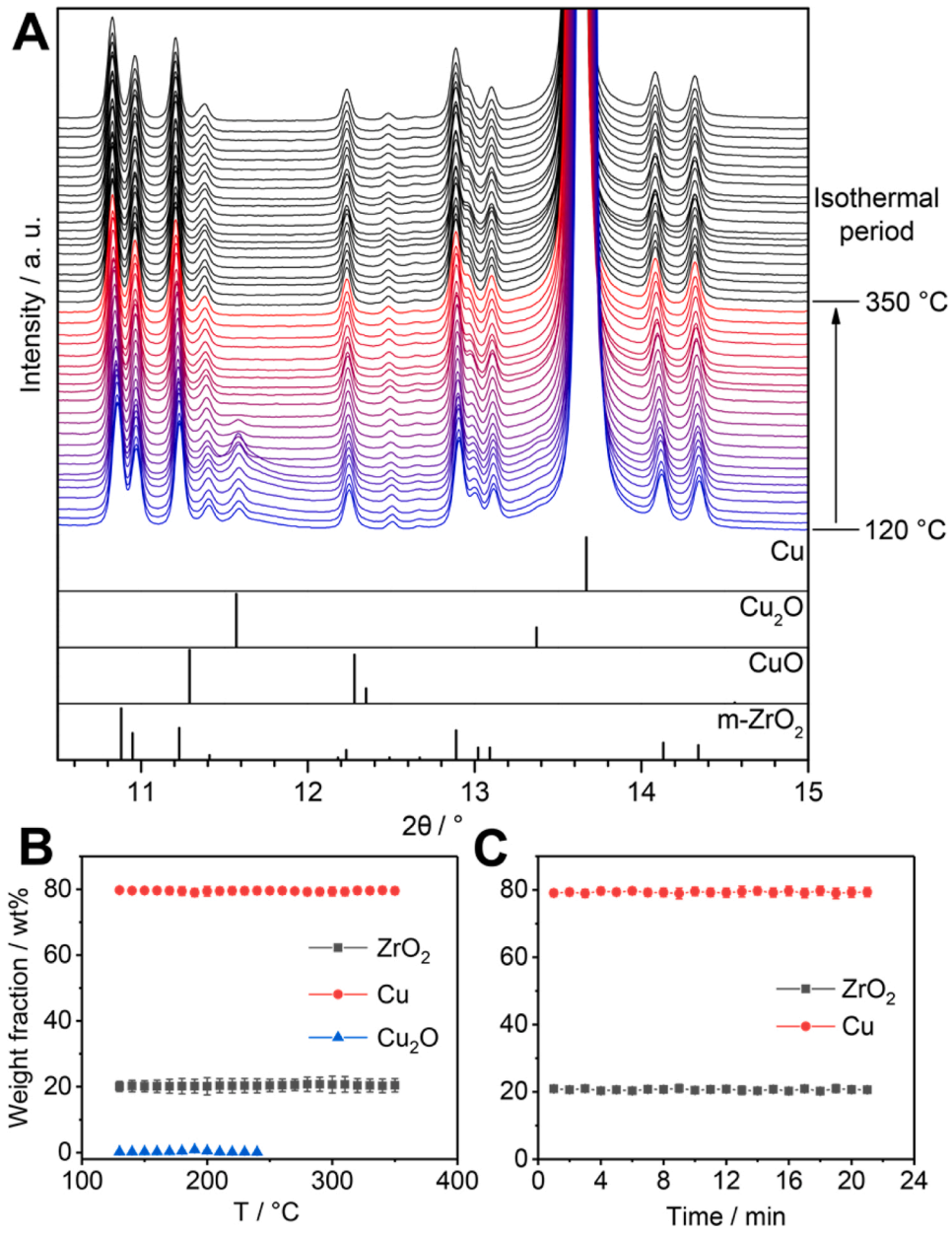


**Fig. 12.** Panel A: *In situ* XRD measurement of CmZ80 in the MSR mixture from 120 °C-350 °C at 25 keV beam energy ($\lambda = 0.4982$ Å). The temperature evolution is color-coded with the heating period as a gradient from blue to red with the isothermal period in black. The reflections of m-$ZrO_2$, Cu, $Cu_2O$ and CuO are marked below. Panels B and C: Composition of the sample during the heating period and the isothermal phase according to RR.

MSR, the occurrence of $Cu_2O$ is correlated with beneficial properties in MSR as an indicator of a temporary super-saturation of Cu with oxygen, providing a non-equilibrium state of Cu [11], especially as direct structural reasons, such as microstrain, can be excluded as discussed above.

The catalytic onset temperatures and the apparent activation energies reveal significant differences in the performance of the catalysts during MSR. The onset temperatures of $H_2$ and $CO_2$ continuously decrease with increasing Cu content accompanied by a continuous increase in the TOFs of $H_2$ and $CO_2$ at 220 °C. A similar trend for the onset temperature can be observed for CO, whereas it increases once more from 40 wt% to 80 wt% Cu. Combined with the lowest onset and highest TOF at 220 °C for $H_2$ and $CO_2$ and the largest extent of the region of > 90 % $CO_2$ selectivity, CmZ80 is identified as the catalyst with the best performance. This implies that the morphology of bulk-like Cu covering and wetting the m-$ZrO_2$ support, providing both an active copper phase and suppressing selectivity-spoiling support-related effects, leads to beneficial properties in MSR.

## 4. Conclusions

As $ZrO_2$ is a particularly suitable support for Cu to steer the methanol steam reforming reaction toward almost 100 % $CO_2$ selectivity, we scrutinized the influence of the Cu-$ZrO_2$ interface- and relative surface dimensions (resulting from Cu loading variation) both on methanol steam reforming activity and selectivity and to identify the associated steering parameters towards high $CO_2$ selectivity.

The variation of Cu metal loading allows steering not only the Cu particle size and the Cu morphology, but also the contribution of potential active sites at the Cu-$ZrO_2$ interface as well as of the intrinsic relative contributions of the support and Cu surface fraction. Based on recent studies, it is clear that $ZrO_2$ is by no means an inactive support

and can therefore influence both the $CO_2$-selective and selectivity-spoiling reaction channels of the overall reaction mechanism. Additionally, the specific $ZrO_2$ surface chemistry is highly preparation-dependent, rendering it difficult to disentangle largely support-specific effects from the special phase-boundary reactivity and the intrinsic Cu° reactivity. By choosing the broad range of Cu loadings, a comparison of the most extreme cases becomes accessible, namely strong predominance of the intrinsic Cu surface area contributions (almost all Cu sites within a bulk-like Cu environment, interfacial and support surface site contributions minimized) *vs.* almost atomic-scale dispersion of Cu, representing the opposite scenario. The combination of low onset temperatures and high TOFs of $H_2$ and $CO_2$ as well as a wide temperature range of $CO_2$ selectivity > 90 % distinguish the Cu/m-$ZrO_2$ catalyst with the highest Cu loading of 80 wt% Cu from all other catalysts with corresponding lower Cu loading. It fulfils the proposed requirements of the presence of support-wetting bulk-like Cu avoiding adverse support effects to directionally enhance the $CO_2$ selectivity. This even holds for a support exhibiting an already relatively low selectivity-spoiling contribution. Hence, we propose that loading variation can be important for any support to distinguish between selectivity-spoiling and -promoting cases, which is also important in view of catalyst design toward CO-depleted reformate gas. As a particular important outcome, we could exclude a predominant dependence of structural effects (change in lattice parameter or microstrain) on the Cu-$ZrO_2$ interfacial dimension and, accordingly, the $CO_2$ selectivity. After focussing on the fundamental issues of the steering parameters for explaining the interfacial Cu-$ZrO_2$ reactivity, future work should be directed at assessing the long-term stability of the Cu-$ZrO_2$ interfaces to infer potential stabilizing factors for structural stability. Furthermore, analysis of the XANES and EXAFS of the samples could provide additional information on the interaction of Cu and $ZrO_2$ [42,43].

## CRediT authorship contribution statement

**Kevin Ploner:** Formal analysis, Investigation, Writing - original draft, Writing - review & editing. **Parastoo Delir Kheyrollahi Nezhad:** Formal analysis, Investigation. **Maximilian Watschinger:** Formal analysis, Investigation. **Lukas Schlicker:** Formal analysis, Investigation. **Maged F. Bekheet:** Formal analysis, Investigation. **Aleksander Gurlo:** Formal analysis, Investigation. **Albert Gili:** Formal analysis, Investigation. **Andrew Doran:** Formal analysis, Investigation. **Sabine Schwarz:** Formal analysis, Investigation. **Michael Stöger-Pollach:** Formal analysis, Investigation. **Johannes Bernardi:** Formal analysis, Investigation. **Marc Armbrüster:** Formal analysis, Investigation, Conceptualization. **Bernhard Klötzer:** Formal analysis. **Simon Penner:** Funding acquisition, Methodology, Project administration, Writing - original draft, Writing - review & editing.

## Declaration of Competing Interest

The authors report no declarations of interest.

## Acknowledgments

The work was financially supported by the Austrian Science Foundation (FWF) under SFB projects F4503-N16 and F4501-N16 and the DACH project I2877-N34. Further support was provided by the framework of the platform Materials- and Nanoscience and the special PhD program “Reactivity and Catalysis” at the University of Innsbruck. The authors additionally thank the Deutsche Forschungsgemeinschaft (DFG) for funding the investigations at the Technische Universität Chemnitz (project AR 617/12-1). L. Schlicker appreciates the ALS for supporting his work with a doctoral fellowship. Financial support by the DFG within the framework of the German Initiative for Excellence is gratefully acknowledged. The authors further thank the Advanced Light Source, a U.S. DOE Office of Science User Facility under contract no. DE-AC02-05CH11231, where *in situ* powder XRD measurements were conducted at the beamline 12.2.2 in the framework of the AP program ALS-08865. We particularly thank the group of H. Huppertz from the Department of General, Inorganic and Theoretical Chemistry of the University of Innsbruck for providing the possibility of using their X-ray diffractometer for *ex situ* powder XRD measurements.

## Appendix A. Supplementary data

Supplementary material related to this article can be found, in the online version, at doi:https://doi.org/10.1016/j.apcata.2021.118279.

## References

[1] G.A. Olah, Angew. Chem. Int. Ed. 52 (2013) 104–107, https://doi.org/10.1002/anie.201204995.
[2] S. Sá, H. Silva, L. Brandão, J.M. Sousa, A. Mendes, Appl. Catal. B 99 (2010) 43–57, https://doi.org/10.1016/j.apcatb.2010.06.015.
[3] P. Preuster, C. Papp, P. Wasserscheid, Acc. Chem. Res. 50 (2017) 74–85, https://doi.org/10.1021/acs.accounts.6b00474.
[4] B. Frank, F. Jentoft, H. Soerijanto, J. Kröhnert, R. Schlögl, R. Schomäcker, J. Catal. 246 (2007) 177–192, https://doi.org/10.1016/j.jcat.2006.11.031.
[5] Z. Baysal, S. Kureti, Appl. Catal. B 262 (2020) 118300, https://doi.org/10.1016/j.apcatb.2019.118300.
[6] H.P. Dhar, L.G. Christner, A.K. Kush, J. Electrochem. Soc. 134 (1987) 3021–3026, https://doi.org/10.1149/1.2100333.
[7] J. Agrell, H. Birgersson, M. Boutonnet, I. Melián-Cabrera, R.M. Navarro, J.L. G. Fierro, J. Catal. 219 (2003) 389–403, https://doi.org/10.1016/S0021-9517(03)00221-5.
[8] K. Narusawa, M. Hayashida, Y. Kamiya, H. Roppongi, D. Kurashima, K. Wakabayashi, JSAE Rev. 24 (2003) 41–46, https://doi.org/10.1016/S0389-4304(02)00239-4.
[9] L. Mayr, B. Klötzer, D. Schmidmair, N. Köpfle, J. Bernardi, S. Schwarz, M. Armbrüster, S. Penner, ChemCatChem 8 (2016) 1778–1781, https://doi.org/10.1002/cctc.201600361.
[10] H. Purnama, F. Girgsdies, T. Ressler, J.H. Schattka, R.A. Caruso, R. Schomäcker, R. Schlögl, Catal. Lett. 94 (2004) 61–68, https://doi.org/10.1023/B:CATL.0000019332.80287.6b.
[11] M. Behrens, M. Armbrüster, in: L. Guczi, A. Erdôhelyi (Eds.), Catalysis for Alternative Energy Generation, Springer, New York, New York, NY, 2012, pp. 175–235.
[12] L. Mayr, X. Shi, N. Köpfle, B. Klötzer, D. Zemlyanov, S. Penner, J. Catal. 339 (2016) 111–122, https://doi.org/10.1016/j.jcat.2016.03.029.
[13] H. Oguchi, H. Kanai, K. Utani, Y. Matsumura, S. Imamura, Appl. Catal. A 293 (2005) 64–70, https://doi.org/10.1016/j.apcata.2005.07.010.
[14] N. Takezawa, M. Shimokawabe, H. Hiramatsu, H. Sugiura, T. Asakawa, H. Kobayashi, React. Kinet. Catal. Lett. 33 (1987) 191–196, https://doi.org/10.1007/BF02066722.
[15] I. Ritzkopf, S. Vukojević, C. Weidenthaler, J.-D. Grunwaldt, F. Schüth, Appl. Catal. A 302 (2006) 215–223, https://doi.org/10.1016/j.apcata.2006.01.014.
[16] H. Bluhm, M. Hävecker, A. Knop-Gericke, E. Kleimenov, R. Schlögl, D. Teschner, V. I. Bukhtiyarov, D.F. Ogletree, M. Salmeron, J. Phys. Chem. B 108 (2004) 14340–14347, https://doi.org/10.1021/jp040080j.
[17] F. Raimondi, K. Geissler, J. Wambach, A. Wokaun, Appl. Surf. Sci. 189 (2002) 59–71, https://doi.org/10.1016/S0169-4332(01)01045-5.
[18] H. Oguchi, T. Nishiguchi, T. Matsumoto, H. Kanai, K. Utani, Y. Matsumura, S. Imamura, Appl. Catal. A 281 (2005) 69–73, https://doi.org/10.1016/j.apcata.2004.11.014.
[19] K. Ploner, M. Watschinger, P. Delir Kheyrollahi Nezhad, T. Götsch, L. Schlicker, E.-M. Köck, A. Gurlo, A. Gili, A. Doran, L. Zhang, N. Köwitsch, M. Armbrüster, S. Vanicek, W. Wallisch, C. Thurner, B. Klötzer, S. Penner, J. Catal. 391 (2020) 497–512, https://doi.org/10.1016/j.jcat.2020.09.018.
[20] WinX$^{POW}$, STOE & Cie GmbH, 2008.
[21] ICDD Database PDF-4+, International Centre for Diffraction Data, Newtown Square, PA 19073, USA, 2010.
[22] C. Prescher, V.B. Prakapenka, High Pressure Res. 35 (2015) 223–230, https://doi.org/10.1080/08957959.2015.1059835.
[23] A. Doran, L. Schlicker, C.M. Beavers, S. Bhat, M.F. Bekheet, A. Gurlo, Rev. Sci. Instrum. 88 (2017) 13903, https://doi.org/10.1063/1.4973561.
[24] L. Schlicker, A. Doran, P. Schneppmüller, A. Gili, M. Czasny, S. Penner, A. Gurlo, Rev. Sci. Instrum. 89 (2018) 33904, https://doi.org/10.1063/1.5001695.
[25] J. Rodriguez-Carvajal, in: FULLPROF: A Program for Rietveld Refinement and Pattern Matching Analysis, Collected Abstract of Powder Diffraction Meeting, Toulouse, France, 1990.
[26] L.W. Finger, D.E. Cox, A.P. Jephcoat, J. Appl. Crystallogr. 27 (1994) 892–900, https://doi.org/10.1107/S0021889894004218.
[27] S. Natesakhawat, J.W. Lekse, J.P. Baltrus, P.R. Ohodnicki, B.H. Howard, X. Deng, C. Matranga, ACS Catal. 2 (2012) 1667–1676, https://doi.org/10.1021/cs300008g.
[28] E.S. Vasiliadou, T.M. Eggenhuisen, P. Munnik, P.E. de Jongh, K.P. de Jong, A. A. Lemonidou, Appl. Catal. B 145 (2014) 108–119, https://doi.org/10.1016/j.apcatb.2012.12.044.

[29] J.W. Evans, M.S. Wainwright, A.J. Bridgewater, D.J. Young, Appl. Catal. 7 (1983) 75–83, https://doi.org/10.1016/0166-9834(83)80239-5.
[30] CasaXPS: Processing Software for XPS, AES, SIMS and More, Casa Software Ltd., 2021.
[31] W.H. Gries, Surf. Interface Anal. 24 (1996) 38–50, https://doi.org/10.1002/(SICI)1096-9918(199601)24:1<38:AID-SIA84>3.0.CO;2-H.
[32] M.K. Dongare, V. Ramaswamy, C.S. Gopinath, A.V. Ramaswamy, S. Scheurell, M. Brueckner, E. Kemnitz, J. Catal. 199 (2001) 209–216, https://doi.org/10.1006/jcat.2001.3173.
[33] S. Tada, S. Kayamori, T. Honma, H. Kamei, A. Nariyuki, K. Kon, T. Toyao, K. Shimizu, S. Satokawa, ACS Catal. 8 (2018) 7809–7819, https://doi.org/10.1021/acscatal.8b01396.
[34] H. Werner, D. Herein, G. Schulz, U. Wild, R. Schlögl, Catal. Lett. 49 (1997) 109–119, https://doi.org/10.1023/A:1019076415303.
[35] K. Pokrovski, K.T. Jung, A.T. Bell, Langmuir 17 (2001) 4297–4303, https://doi.org/10.1021/la001723z.
[36] R.A. Köppel, C. Stöcker, A. Baiker, J. Catal. 179 (1998) 515–527, https://doi.org/10.1006/jcat.1998.2252.
[37] J. Liu, J. Shi, D. He, Q. Zhang, X. Wu, Y. Liang, Q. Zhu, Appl. Catal. A 218 (2001) 113–119, https://doi.org/10.1016/S0926-860X(01)00625-1.
[38] H.F. McMurdie, M.C. Morris, E.H. Evans, B. Paretzkin, W. Wong-NG, C.R. Hubbard, Powder Diffr. 1 (1986) 40–43, https://doi.org/10.1017/S0885715600011271.
[39] H.E. Swanson, E. Tatge, Natl. Bur. Stand. (US) Circ. 539 (1) (1953) 15.
[40] N.E. Brese, M. O'Keeffe, B.L. Ramakrishna, R.B. von Dreele, J. Solid State Chem. 89 (1990) 184–190, https://doi.org/10.1016/0022-4596(90)90310-T.
[41] R. Restori, D. Schwarzenbach, Sec. B: Struct. Sci. 42 (1986) 201–208, https://doi.org/10.1107/S0108768186098336.
[42] T. Witoon, J. Chalorngtham, P. Dumrongbunditkul, M. Chareonpanich, J. Limtrakul, Chem. Eng. J. 293 (2016) 327–336, https://doi.org/10.1016/j.cej.2016.02.069.
[43] A. Szizybalski, F. Girgsdies, A. Rabis, Y. Wang, M. Niederberger, T. Ressler, J. Catal. 233 (2005) 297–307, https://doi.org/10.1016/j.jcat.2005.04.024.